Atmos. Meas. Tech., 15, 845–877, 2022
https://doi.org/10.5194/amt-15-845-2022

Atmospheric Measurement Techniques
Open Access
EGU

Retrieval of UV–visible aerosol absorption using AERONET and OMI–MODIS synergy: spatial and temporal variability across major aerosol environments

Vinay Kayetha[1,2], **Omar Torres**[2], **and Hiren Jethva**[2,3]

[1]Science Systems and Applications Inc., Lanham, Maryland 20706, USA
[2]NASA Goddard Space Flight Center, Greenbelt, Maryland 20771, USA
[3]Universities Space Research Association, Columbia, Maryland 21046, USA

Correspondence: Vinay Kayetha (vinay.k.kayetha@nasa.gov)

Received: 10 January 2021 – Discussion started: 19 January 2021
Revised: 19 December 2021 – Accepted: 21 December 2021 – Published: 18 February 2022

Abstract. Measuring spectral aerosol absorption remains a challenging task in aerosol studies, especially in the UV region, where ground and airborne measurements are sparse. In this paper, we introduce an algorithm that synergizes ground measurements with satellite observations for the derivation of spectral single scattering albedo (SSA, ω_o) of aerosols in the UV-to-visible wavelength range (340–670 nm). The approach consists in explaining satellite-measured near-UV radiances (340, 354, 388 nm) by the Ozone Monitoring Instrument (OMI) and visible radiances (466, 646 nm) by the Moderate Resolution Imaging Spectroradiometer (MODIS), given the collocated ground-based Aerosol Robotic Network (AERONET) measurements of total column extinction aerosol optical depth (AOD, τ), in terms of retrieved total column wavelength-dependent SSA using radiative transfer calculations. Required information on aerosol particle size distribution is adopted from AERONET-based aerosol type-dependent seasonal climatologies specifically developed for this project. The inversion procedure is applied to about 110 AERONET sites distributed worldwide, for which continuous, long-term AERONET measurements are available. Using the derived data set, we present seasonal and regional climatology of $\omega_o(\lambda)$ for carbonaceous, dust, and urban/industrial aerosols. The resulting UV–visible spectral dependence of ω_o obtained for these three major aerosol types is found to be both qualitatively and quantitatively consistent with independent measurements reported in the literature. A comparison to standard AERONET SSA product at 440 nm shows absolute differences within 0.03 (0.05) for 40 % (65 %) of the compared observations. The derived aerosol $\omega_o(\lambda)$ data set provides a valuable addition to the existing aerosol absorption record from AERONET by extending it to the near-UV region. Furthermore, SSA retrievals from our method at visible wavelengths and around satellite overpass time also complement the equivalent inversion available during early morning/late afternoon from AERONET. In addition to improving our understanding of spectral aerosol absorption properties, the combined UV–visible data set also offers wavelength-dependent dynamic aerosol absorption models for use in the satellite-based aerosol retrieval algorithms.

1 Introduction

Through scattering and absorption of solar radiation, atmospheric aerosols play a significant role in the radiation balance of the Earth's climate system. The ratio of the amount of the light scattering to the total extinction is referred to as single scattering albedo (SSA, ω_o). It is a fundamental variable used to gauge the absorbing nature of aerosols. Mie theory indicates the value of ω_o is 1.0 for purely scattering aerosols and less than 1 towards 0 for the increasingly absorbing nature of aerosols. Studies show that the estimates of net aerosol radiative forcing are sensitive to the aerosol ω_o, and small changes to it could potentially alter the forcing on atmosphere (Chyacutelek and Coakley, 1974; Hansen et al., 1997). General circulation models are often fed with

essential aerosol properties to estimate the aerosol radiative forcing effects on the atmosphere. These properties include aerosol optical depth (AOD, τ), complex refractive index, and scattering phase function. Here, the knowledge on spectral dependence of such properties is crucial in quantifying the overall effects of aerosols. For example, absorbing aerosols can lead up to a 50 % decrease in the near-UV solar irradiance compared to the similar load of only scattering aerosols in the atmosphere (Bais et al., 2005). A report by the Intergovernmental Panel on Climate Change (IPCC) suggests that the lack of data on spectral aerosol absorption is one of the major contributors, leading to significant uncertainties in quantifying the net aerosol radiative effects on the Earth's climate (IPCC, 2013).

Developments in ground-based and satellite aerosol retrieval techniques have greatly improved our understanding of atmospheric aerosols over the last two decades. However, knowledge on spectral aerosol absorption properties is limited due to difficulties in measurements (e.g., Heintzenberg et al., 1997) and larger uncertainties in remote sensing retrievals (e.g., Dubovik et al., 2000). Direct measurements of aerosol absorption can be obtained by using instruments that measure aerosol scattering and extinction coefficients. Such measurements are limited to discrete wavelengths and associated with fewer ground stations, laboratory measurements, or airborne field campaigns. In addition, in situ techniques often require making corrections of measurements to overcome instrumental challenges (e.g., Weingartner et al., 2003; Virkkula et al., 2005; Collaud Coen et al., 2010). Aerosol absorption can also be inferred from the combined sky radiance and extinction measurements that rely on fitting ground observations to radiative transfer calculations (Nakajima et al., 1996; Dubovik et al., 1998; Cattrall et al., 2003). The accuracy of the aerosol absorption retrieval through ground-based remote sensing techniques primarily relies on the instrument calibration, whereas ancillary information such as the characterization of surface reflectivity has only a secondary effect on the overall accuracy of the retrievals. Detailed reviews of measurements and techniques to retrieve aerosol absorption are available in the literature (e.g., Clarke et al., 1967; Bond and Bergstrom, 2006; Moosmüller et al., 2009). Among ground-based sensors, AERONET (Aerosol Robotic Network) provides the longest aerosol absorption record at four discrete wavelengths from the visible (Vis) to near-infrared (NIR) spectral region over many sites distributed worldwide. A known limitation of the currently available AERONET inversion product (version 3) is the lack of single scattering albedo at near-UV wavelengths and the aerosol load threshold ($\tau_{440} > 0.4$) required to obtain reliable absorption in the Vis–NIR spectrum. Like AERONET, a ground-based radiation measurement network with sites in Asia and Europe referred to as SKYNET (Sky Radiometer Network) provides aerosol optical depth and single scattering albedo in the near-UV–NIR spectrum (Nakajima et al., 2007). However, the accuracy of the SKYNET aerosol absorption product is affected by temporally constant and spectrally invariant surface reflectance used in the inversion procedure (Jethva and Torres, 2019). These limitations restrict our ability of complete characterization of aerosol absorption as a function of both wavelength and aerosol load.

For a few decades now, satellite remote sensing has been used as an essential tool to gain a global perspective of aerosols distribution in the atmosphere. The physical basis of satellite aerosol retrievals is that under cloud-free conditions after accounting for Rayleigh (molecular) scattering, gaseous absorption effects, and surface reflectance, the upwelling top-of-the-atmosphere (TOA) reflectance is a function of aerosol optical depth, particle size, and composition (i.e., complex refractive index). Mathematically, for a cloud-free atmosphere overlying an Lambertian surface the upwelling TOA reflectance (L_{TOA}) received by a nadir-viewing satellite can be expressed in normalized units as (Chandrasekhar, 1960):

$$L_{\mathrm{TOA}}(\theta,\varphi,\lambda) = L_0(\theta,\varphi,\lambda) + \frac{\rho(\lambda)\cdot T(\tau,\theta,\lambda)}{(1-s(\lambda)\cdot\rho(\lambda))}, \quad (1)$$

where θ, φ, and λ are the zenith, azimuthal angles of the direction of propagation and wavelength of light, L_0 is the atmospheric path radiance, τ is the optical thickness of the atmosphere, ρ is the surface reflectivity, T is the total direct and diffuse transmittance of the light in the atmosphere, and $s(\lambda)$ is the spherical albedo of the atmosphere when it is illuminated from below.

The first and second terms on the right side of Eq. (1) represent the atmospheric path radiance and the amount of light that is reflected to the sensor after encountering the surface, respectively. The satellite-measured TOA reflectances are sensitive to both τ and ω_{o}, in addition to the surface reflectance. Therefore, separating the contributions of atmosphere and surface is of utmost importance to retrieve aerosols from satellite measurements. For satellites with single-view measurements, aerosol retrieval algorithms rely on prior assumptions on particle sizes (scattering phase function) and ω_{o} to retrieve τ. On the other hand, several efforts have been made to estimate aerosol ω_{o} from direct satellite measurements at visible wavelengths (e.g., Kaufman, 1987; Kaufman et al., 2002; Satheesh and Srinivasan, 2005; Zhu et al., 2011) and near-UV wavelengths (Torres et al., 1998, 2007, 2013). However, the variety of natural surface types, choice of wavelengths, and aerosol models pose limitations on such techniques. In terms of wavelength, enhanced molecular scattering in the near-UV region acts as a strong attenuating background below the aerosol layer and helps identify absorbing aerosols. However, to retrieve aerosol absorption using near-UV measurements, quantitative information on aerosol layer height (ALH) is required. Existing satellite aerosol retrieval techniques that rely on observations in the visible spectrum assume a temporally constant value of ω_{o} that varies regionally (Remer et al., 2005; Levy et al., 2007), and for a few algorithms, it is still assumed to be wavelength-independent (Hsu et al., 2013). A review of commonly used

satellite aerosol products singled out aerosol absorption as an inherent problem common to all sensors (Li et al., 2009). Studies using the evolving ground-based aerosol record provide evidence that satellite-retrieved τ can lead to large biases if the assumed aerosol imaginary index, which drives ω_o, is wavelength-independent (Jethva and Torres, 2011) and seasonally invariant (Lyapustin et al., 2011; Eck et al., 2013). These studies highlight the importance of using wavelength-dependent aerosol ω_o and accounting for its spatial and temporal variability in the retrieval of satellite aerosol products.

In the past, few studies used both ground and satellite measurements to retrieve aerosol absorption properties. Li et al. (1999) used visible band radiances from AVHRR (Advanced Very High Resolution Radiometer) and in situ-measured τ during the SCAR-B (Smoke, Clouds, and Radiation–Brazil) experiment to derive absorption from biomass burning aerosols. Sinyuk et al. (2003) used UV radiances from TOMS (Total Ozone Monitoring Station) and aerosol extinction from AERONET to derive the imaginary refractive index of dust particles over a few stations in the Saharan region. Lee et al. (2007) estimated the aerosol SSA across a few stations over China using combined ground and satellite (MODIS, Moderate Resolution Imaging Spectroradiometer) measurements at visible wavelengths. Nonetheless, these studies are limited and do not provide a comprehensive, long-term characterization of absorbing aerosols in the UV–visible spectral region.

The objectives of the present work are to derive columnar aerosol $\omega_o(\lambda)$ and its spectral dependence in the UV–visible part of the spectrum. The proposed inversion procedure makes use of AERONET-measured wavelength-dependent τ and retrieved particle size distribution in conjunction with satellite-measured radiances at UV and visible wavelengths by A-train constellation sensors Aura OMI (Ozone Monitoring Instrument) and Aqua MODIS. The near-simultaneous measurements from these sensors provide an excellent opportunity to combine satellite and ground measurements during the overpass times (local time, $\sim$13:30 LT) over the AERONET sites.

The organization of the paper is as follows: Sect. 2 describes the ground-based and satellite measurements used in this work; Sect. 3 describes the methodology adopted to derive aerosol $\omega_o(\lambda)$; Sect. 4 discusses results of sensitivity analysis aimed at estimating the expected accuracy of the proposed aerosol absorption retrievals; Sect. 5 presents a comparison of the resulting SSA product from this work to the AERONET aerosol absorption product; Sect. 6 presents the seasonal variability in regional aerosol $\omega_o(\lambda)$ derived for sites across major aerosol environments worldwide; Sect. 7 provides a discussion of the regional variability of the UV–Vis aerosol absorption product derived in this work. Finally, Sect. 8 provides a summary of the work, along with the key findings and outlook for further studies.

2 Data sets

The details of ground-based and satellite data sets used in this work are provided in Table 1. Our usage of satellite data is strictly limited to the measured TOA reflectances by the Aqua-MODIS and Aura-OMI sensors, the associated viewing geometry, and other ancillary information such as quality flags (QFs) and the OMI near-UV aerosol index (UVAI).

2.1 AERONET

AERONET employs an automatic sun-tracking photometer (Cimel Electronique CE-318) to measure sun and sky radiances (Holben et al., 1998). The direct sun measurements are made with a 1.2° full field of view at nine nominal wavelengths of 340, 380, 440, 500, 675, 870, 940, 1020, and 1640 nm typically for every $\sim$ 5 to 15 min interval. Columnar extinction τ is computed from these measurements for all wavelengths except for the 940 nm, which is used to retrieve water vapor amounts. The extinction τ obtained from these measurements has an estimated uncertainty of $\pm$0.01 ($\pm$0.02) at the visible (near-UV) wavelengths, primarily due to calibration uncertainty (Eck et al., 1999). The currently available AERONET version 3 level 2 AOD product uses improved cloud screening and quality checks to provide reliable data to the user community (Giles et al., 2019). In addition to the direct sun measurements, the photometer also measures multi-angular diffuse sky radiances along the almucantar plane (plus hybrid scans to lower solar zenith angles) at four distinct wavelengths from the visible to the near-infrared spectrum (440, 675, 870, and 1020 nm) with near-hourly frequency. In recent years the newer model of instruments also include sky radiance measurements at 380, 500, and 1640 nm (Sinyuk et al., 2020). An inversion procedure that uses both direct sun and angular sky radiances together is implemented to derive aerosol particle size distribution and complex refractive indices (Dubovik and King, 2000; Dubovik et al., 2006). The uncertainty in the derived spectral aerosol SSA provided by the AERONET inversion level 2 product is estimated to be $\pm$0.03 for $\tau_{440} > 0.4$ (Dubovik et al., 2000). Since 2018, the release of the version 3 inversion product has implemented several changes to the traditional AERONET aerosol absorption retrievals. A complete description of the changes implemented in version 3 inversion products along with the updated uncertainty estimates is available in Sinyuk et al. (2020). It should be noted here that in the currently available AERONET inversion products the shortest wavelength of aerosol SSA is 440 nm. In this work, we use the AERONET version 2 inversion product for constructing a representative aerosol model for the associated sites. For the AOD inputs to our retrieval algorithm and for the comparison of SSA we use the latest version 3 products. Figure 1 shows the location of the total 110 AERONET sites selected in this work for which long-term ($>$ 7 years) quality-assured measurements are available.

Table 1. Description of the ground and satellite data products used in this work.

Purpose	Instrument	Product	Level and version	Parameter(s)
For SSA retrieval in this work	AERONET	AOD	L2, V3	AOD and extinction Ångström exponent.
		Inversion	L2, V2	Particle size distributions, and real part of refractive index at 440 nm.
	OMI	OMLERWAVE, OMAERUV	L2, V1.8.9.1	TOA reflectances (with QFs), aerosol type, LER, aerosol layer height obtained from CALIPSO.
	MODIS	MYD04	L2, C006	TOA reflectances (with QFs) provided by the Deep Blue algorithm.
		MAIAC-MCD19A1	L2, C006	Surface reflectance at 466 and 646 nm.
Comparison	AERONET	Inversion	L2, V3	SSA at 440 and 675 nm.

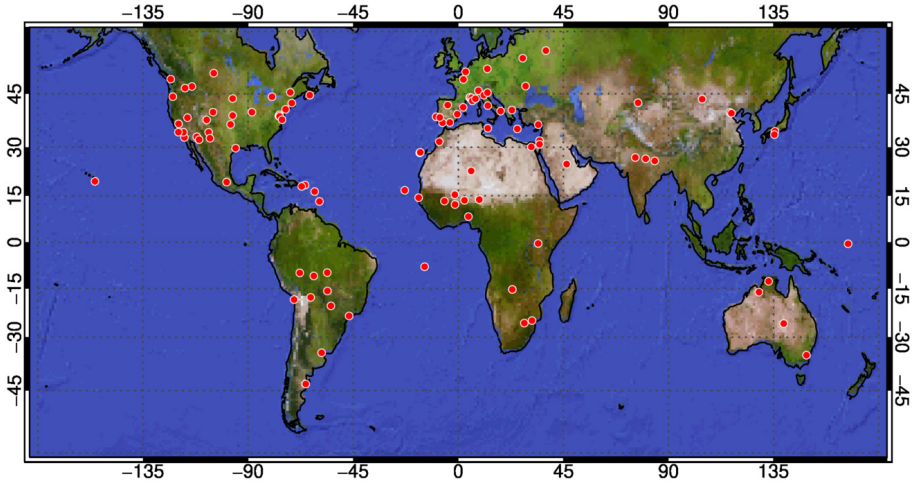

Figure 1. The geo-distribution of AERONET sites whose AOD data are used for the retrieval of spectral aerosol single scattering albedo in this work.

2.2 OMI

Launched in July 2004, the OMI on board NASA's Earth Observing System (EOS) Aura satellite is a nadir-viewing hyper-spectral imaging radiometer (Levelt et al., 2006). OMI measures the TOA radiances in the wavelength range 270–500 nm with a ground pixel spatial resolution of 13 km × 24 km at nadir. OMI achieves daily global coverage in 14–15 orbits with a swath of 2600 km scanning the entire Earth's surface. In this work, we use OMI radiances (340, 354, and 388 nm) provided in the in-house product OMLERWAVE and publicly accessible OMI near-UV OMAERUV level 2 aerosol product (version 1.8.9.1, Torres et al., 2018). The OMLERWAVE product reports radiances and Lambertian equivalent reflectivity (LER) at several discrete wavelengths in the near-UV and visible parts of the spectrum. Additionally, we also use ancillary information on the quality of pixel (cloud contamination, land/sea mask, etc.), UVAI, LER, surface pressure, and ALH data set used in the operational OMAERUV product. Since mid-2007, OMI has suffered from an external obstruction that affects the quality of radiance measurements in a few rows (cross-track pixels). This is referred to as the "row anomaly" that restricts the current usage of OMI observations for scientific purposes to about half in a total of 60 cross-track rows (Schenkeveld et al., 2017). The impact of reduced spatial coverage as a result of the row anomaly on the OMAERUV aerosol product is discussed by Torres et al. (2018).

2.3 MODIS

The MODIS sensor on board NASA's EOS Aqua and Terra satellites is a nadir-viewing, multi-spectral radiometer. MODIS measures the TOA radiances in 36 wavelength bands ranging from 0.41–14.23 µm with a ground pixel spatial resolution between 250–1000 m (King et al., 1992).

MODIS scans the Earth's surface with a 2300 km wide swath to provide near-global coverage daily. In this work, we use Aqua-MODIS radiances (at 466 and 646 nm) provided in the 10 km aerosol product (MYD04_L2) from the Deep Blue (DB) aerosol algorithm. This aerosol product provides cloud-free radiances and ancillary information on the terrain height/pressure, quality of pixel, and estimated cloud fraction (Hsu et al., 2013). For surface characterization in visible wavelengths we use the MODIS MAIAC (Multi-Angle Implementation of Atmospheric Correction) MCD19A1 daily 1 km sinusoidal gridded spectral BRF (bidirectional reflectance function) or surface reflectance product (Lyapustin and Wang, 2018).

3 Methodology

A schematic flowchart shown in Fig. 2 illustrates the method adopted in this work to derive wavelength-dependent aerosol single scattering albedo.

3.1 Computation of site-specific seasonal lookup tables of TOA reflectances

To start, we compile a seasonal climatology of aerosol particle size distributions and the real part of the refractive index (440 nm) for the entire τ range from the AERONET level 2, version 2 inversion product for each site considered in the study (see Fig. 1). Here, we assume that the spectral variability of the real part of the aerosol refractive index through UV–visible is minimal, and, therefore, values derived at 440 nm were assumed to be wavelength-independent across the UV–visible spectral range considered in this study. The resulting site-specific climatologies of aerosol size distribution are fed to a radiative transfer model (RTM) to generate lookup tables (LUTs) of outgoing TOA reflectances at 340, 354, 388, 466, and 646 nm with varying nodal points of satellite–sun geometry (i.e., SZA – solar zenith angle at 0, 20, 40, 60, 66, 72, and 80°; VZA – viewing zenith angle at 2° interval from 0–88°; RAA – relative azimuth angle at 15° interval from 0–180°). Reflectance LUTs are created for two values of surface pressure (1013.25 and 600 mbar), seven values of τ (0.0, 0.1, 0.5, 1.0, 2.5, 4.0, and 6.0), five nodal points on ALH (0, 1.5, 3.0, 6.0, and 10.0 km) for the referenced surface pressure nodes, and eight values of the imaginary component of the refractive index (0.000, 0.008, 0.016, 0.024, 0.032, 0.040, 0.048, and 0.056). The aerosol profiles used in the RTM follow a Gaussian distribution centered around the respective modes of ALH. We assumed a total column ozone of 275 DU (Dobson unit) in the RTM to account for ozone absorption. The Gauss–Seidel radiative transfer code used for the radiative transfer simulations accounts for gaseous absorption (NO_2 is not included), as well as molecular and aerosol multiple scattering (Herman and Browning, 1965). Thus, a database of AERONET site-specific seasonal LUTs of reflectances for the aerosols observed over each site in the study is created. Figure 3 shows an example of the calculated net aerosol reflectance at the TOA for selected sun–satellite geometry (SZA = 20°, VZA = 40°, RAA = 130°) and varying values of τ and ω_o from our LUT developed for the Goddard Space Flight Center (GSFC) site (38.92° N, 76.84° W). These results illustrate that for a given satellite–sun geometry, observed radiance, and assumed LUT, multiple combinations of τ and ω_o can explain the satellite measurements. In addition, it is noted that the net reflectances are mostly invariant at low optical depths (~ 0.1) regardless of variations in SSA for all wavelengths. This is a typical scenario for the LUT approach to derive aerosol properties, suggesting retrieval of absorption is likely not reliable at low optical depths. These results also illustrate the critical reflectance concept (Kaufman, 1987) as a particular upwelling reflectance value (also associated with a particular value of surface reflectance) at which there is no sensitivity to aerosol optical depth and which is, therefore, theoretically suitable for the retrieval of aerosol absorption from satellite observations. Nonetheless, to derive the best-fit or unique solution of ω_o from satellite measurements, an accurate characterization of τ, cloud-free radiances, and surface reflectances is required.

The site-specific LUTs developed here assume spherical particle shapes (Mie theory) for carbonaceous and urban aerosols. However, mineral dust particles are assumed to be non-spherical and modeled as randomly oriented spheroids (Dubovik et al., 2006; Torres et al., 2018). To account for the non-sphericity of dust particles, a unified dust model LUT is created using particle sizes from selected AERONET sites over the Sahara and Middle East region that include Saada, SEDE_BOKER, Solar_Village, and Tamanrasset_INM. These sites were selected based on the observed prevailing dust aerosol type. The particle sizes and real refractive index obtained at these sites are used with a precomputed set of kernels that assume a spheroidal shape with a fixed distribution of axis ratio to produce phase function (Dubovik et al., 2006). The obtained phase matrix elements are input to the RTM to create reflectance LUTs. The process of acquiring a non-spherical unified model LUT is necessary to save a considerable computational time, which otherwise would require the creation of another set of site-specific LUTs.

3.2 Collocation of satellite and ground measurements

We use satellite measurements located within the 50 km radius of each AERONET site. In essence, we treat the overlying atmospheric aerosols within a 50 km radius of the site as a representative of the AERONET-measured τ. We look for valid AERONET τ measurements within ± 2 h of satellite overpass and assign the τ closest in time to all the ground pixels. It should be noted here that for the OMI sensor, the OMAERUV product provides cloud-free radiances (340, 354, and 388 nm) in the native pixel resolution of 13 km ×

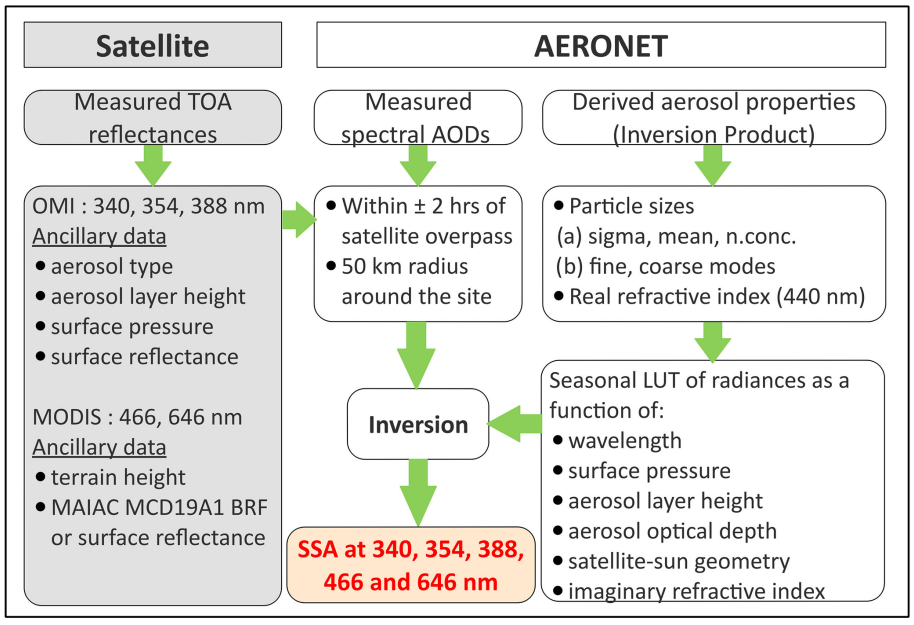

Figure 2. Schematic flowchart of the methodology used to retrieve aerosol spectral single scattering albedo.

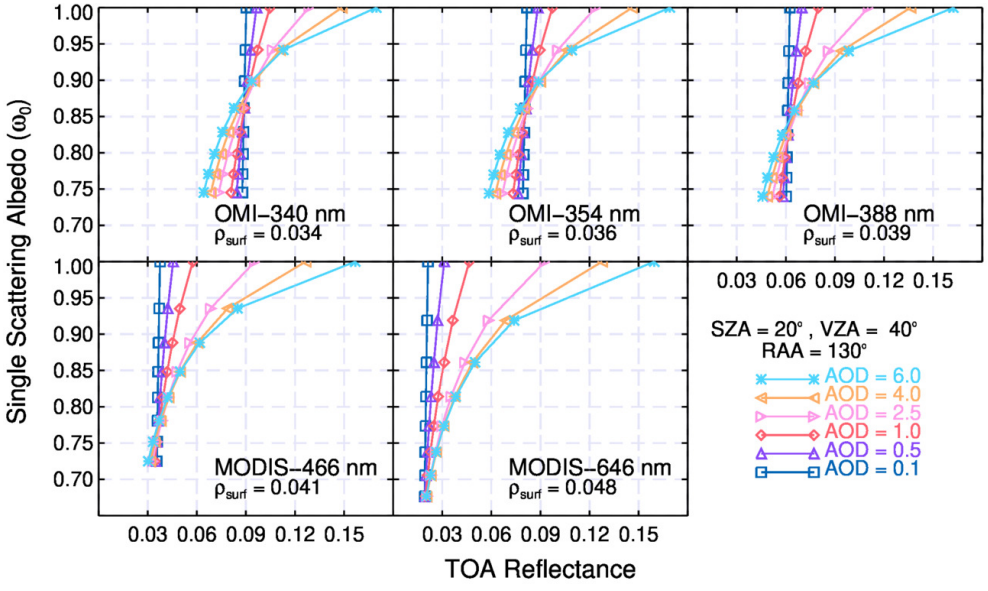

Figure 3. Simulated TOA radiances for the aerosols over the GSFC site as a function of τ and SSA in the UV–visible range.

24 km, while the MODIS sensor DB product provides cloud-free radiances (466 and 646 nm) at 10 km × 10 km resolution.

3.3 Retrieval of aerosol $\omega_0(\lambda)$

The proposed technique to derive aerosol absorption involves obtaining (a) the AERONET AOD at OMI and MODIS wavelengths, (b) aerosol type, (c) aerosol centroid layer height, (d) surface pressure, (e) surface reflectance, and (f) best quality-assured MODIS and OMI-measured cloud free-TOA reflectances.

3.3.1 AERONET AOD at sensor wavelengths

The AODs at the nominal wavelengths measured by AERONET along with the computed extinction Ångström exponent (EAE, α) for several wavelength ranges (340–440, 380–500, 440–675, 440–875, etc.) are available in the AERONET AOD product. We derive the τ at our interest of satellite wavelengths using the closest available measurement and α through the power-law approximation (Ångström, 1929) as shown in Eq. (2). For OMI wave-

lengths, the AERONET 340 and 380 nm measurements are readily available, while τ_{354} is obtained with $\lambda_{\mathrm{Ref}} = 380$ nm and $\alpha_{\lambda_{\mathrm{Ref}}} = \alpha_{340-440}$. For the few sites with older models of the AERONET sun photometer that does not have direct sun measurements at 340 and 380 nm (i.e., Banizoumbou, Avignon, etc.), we use $\lambda_{\mathrm{Ref}} = 440$ nm and $\alpha_{\lambda\_\mathrm{Ref}} = \alpha_{440-675}$. Similarly, for MODIS wavelengths the τ values at 466 and 646 nm are obtained using $\lambda_{\mathrm{Ref}} = 440$ nm and $\alpha_{\lambda\_\mathrm{Ref}} = \alpha_{440-675}$.

$$\tau_{\lambda} = \tau_{\lambda_{\mathrm{Ref}}} \left(\frac{\lambda}{\lambda_{\mathrm{Ref}}} \right)^{-\alpha_{\lambda\_\lambda_{\mathrm{Ref}}}} \quad (2)$$

3.3.2 Aerosol type and ALH

Aerosol type information is essential to derive absorption properties. We use a combination of extinction Ångström exponent ($\alpha_{440-870}$) derived from AERONET and UVAI from OMAERUV product to categorize the observed aerosols into three basic types – dust, carbonaceous, and urban/industrial. Initially, our algorithm uses $\alpha_{440-870}$ to identify the aerosols as coarse ($\alpha_{440-870} \leq 0.2$) and fine ($\alpha_{440-870} \geq 1.2$) mode dominated particles. The threshold $\alpha_{440-870}$ of 0.2 chosen for coarse-mode particles unambiguously identifies dust aerosols. However, the sample of fine-mode particles consists of both carbonaceous and urban types of aerosols that have a wide range of absorption depending on the source of emissions. The near-UV aerosol index is an excellent indicator to identify the presence of absorbing aerosols. The threshold UVAI value adopted from OMAERUV algorithm is used to separate carbonaceous (UVAI ≥ 0.8) and urban (UVAI < 0.8) aerosols, respectively. Based on extensive tests on the OMI signal strength on all surface types it is determined that a minimum UVAI of 0.8 is required to identify absorbing aerosols (Torres et al., 2007, 2013). Although UVAI is an excellent indicator to identify the presence of absorbing aerosols, the large OMI footprint (13 km × 24 km) and sub-pixel contamination may occasionally produce an underestimated UVAI, resulting in the misidentification of the observed aerosols as urban type. To derive aerosol absorption for dust, a LUT for non-spherical particle shape is selected, while for carbonaceous and urban aerosols site-specific spherical LUTs are used. In addition, for the absorbing types of aerosols, i.e., carbonaceous and dust, we choose an estimate of ALH from a CALIOP (Cloud-Aerosol Lidar with Orthogonal Polarization) based ALH climatology product of absorbing aerosols (Torres et al., 2013). Prescribed uncertainty in the monthly climatology of ALH derived from the joint OMI–CALIOP product primarily due to limited sampling of the CALIOP lidar overpasses in the 1° grid (16 d overpass cycle), and day-to-day variability of ALH is expected to be within ±1 km (Torres et al., 2013). For urban aerosols, an exponential aerosol profile peaking at the surface is employed to perform the inversion procedure.

3.3.3 Surface reflectance and pressure

For the surface characterization at OMI wavelengths, we use a near-UV surface albedo database at 0.25° grid resolution provided in the OMAERUV product (Torres et al., 2007). The near-UV surface albedo employed by OMAERUV is derived from minimum Lambertian equivalent reflectance obtained from available long-term measurements. The uncertainty in the near-UV surface albedo from these measurements is expected to be within ±0.01 (Torres et al., 2018). At MODIS wavelengths, the surface reflectance or BRF provided by the MAIAC MCD19A1 product is used. The MAIAC MCD19A1 provides spectral surface BRF over cloud-free and clear-to-moderately-turbid atmospheric conditions ($\tau_{466} < 1.5$) for solar zenith angles below 80°. The measurement-based uncertainty in MCD19A1 BRF at visible wavelengths is reported to be in the range of 0.002–0.003 for the combined sources of errors including uncertainties from gridding, cloud detection, and aerosol model properties (Lyapustin et al., 2018). Additionally, the surface or terrain pressure reported in the OMAERUV and terrain height (converted to pressure) reported in the MODIS aerosol products are used in our SSA retrievals.

Our retrieval technique gathers all the above-mentioned required inputs including the best quality-assured cloud-free radiances reported in OMAERUV (QF = 0) and MODIS-DB (QF = 3) products to perform an inversion for each wavelength independently. The inversion procedure interpolates the LUT radiances linearly for the prescribed satellite–sun geometry, ALH, and τ and logarithmically over the surface pressure nodes. The obtained LUT radiances as a function of the imaginary refractive index are then fitted with the satellite-measured radiances to derive aerosol $\omega_{\mathrm{o}}(\lambda)$.

3.3.4 Correction accounting for NO_2 gas absorption

Among the trace gases present in the lower atmosphere, ozone (O_3) and nitrogen dioxide (NO_2) have strong absorption lines in the UV–visible spectral region of our interest (340–646 nm). As mentioned in Sect. 3.1, the RT model employed in this work accounts for H_2O and O_3 amounts, leaving the simulated radiances with NO_2 absorption unaccounted for. In general, NO_2 amounts present in the lower atmosphere are primarily formed through vehicular and industrial emissions in addition to the small amounts of NO_2 through biomass burning emissions. Therefore, over the regions with high vehicular and industrial emissions, the retrievals of aerosol SSA could be biased since our simulated radiances do not include the contribution from NO_2 amounts. Krotkov et al. (2005) investigated the effect of NO_2 amounts on the retrieval of aerosol SSA using the measured NO_2, aerosol optical depth, and radiance measurements from the UV multifilter rotating shadow-band radiometer (UV-MFRSR). This study demonstrates that at UV wavelengths the aerosol SSA could be biased low due to unaccounted

NO_2 gas absorption in the measured radiances and provides a correction (Eq. 3) to obtain the corrected aerosol single scattering albedo.

$$\omega_a = \omega\,(\text{no NO}_2\text{ corr}) \cdot \left[1 + \frac{\tau_{NO_2}}{\tau_a}\right], \quad (3)$$

where ω_a is the corrected aerosol SSA, ω is the aerosol SSA with NO_2 absorption unaccounted for, τ_{NO_2} is the optical depth of columnar NO_2 amounts, and τ_a is the aerosol optical depth after correcting for Rayleigh and trace gases including NO_2.

For the SSA retrievals in this work, we apply NO_2 gas correction as a final step in our retrieval algorithm. We use NO_2 concentration provided in the AERONET AOD product (determined from monthly climatology of the total column NO_2 retrievals from OMI measurements gridded at $0.25° \times 0.25°$ spatial resolution) and absorption coefficients from Vandaele et al. (1998) to determine τ_{NO_2}. The obtained spectral τ_{NO_2} is used to estimate the corrected aerosol SSA (shown in Eq. 3) as demonstrated by Krotkov et al. (2005).

3.3.5 Illustration of retrieved SSA

Figure 4 shows the retrieved aerosol SSA over the GSFC site as a function of AERONET-measured τ. Located in the vicinity of a metropolitan area, the prevailing aerosols over the GSFC site are the urban industrial types that are relatively more scattering in nature. In general, retrieved SSA increases with aerosol loading, except for a small decrease at large AODs at 466 and 646 nm. Particularly notable is the high variability of retrieved SSA in most τ bins for the visible wavelengths (i.e., MODIS bands). This is due to the diminishing aerosol signal strength for weakly absorbing urban type aerosols at lower aerosol loading in the visible spectrum, where the measured TOA radiances are dominantly contributed by the underlying surface, notably at 646 nm. The mean aerosol SSA retrieved at the GSFC site for observations with $\tau_{440} > 0.4$ at 340, 354, 388, 466, and 646 nm are 0.95, 0.96, 0.96, 0.95, and 0.93, respectively. These results agree well with the values reported for the GSFC site using AERONET products at 440 and 675 nm as 0.96 and 0.95, respectively (Giles et al., 2012). Also shown in Fig. 4 is the number of collocated observations that were used in the inversion and the percent of observations for which SSA is retrieved. For about 12 years of the satellite and ground collocated observations used here, the number of observations from OMI is less than MODIS observations. The difference in the number of collocated observations stems partly from the OMI row anomaly, cloud contamination, and the coarser pixel resolution. The percent of SSA retrieved observations varies widely even within the corresponding sensor wavelengths (OMI: 340, 354, and 388 nm; MODIS: 466 and 646 nm). At times depending on the surface reflectance, the computed net aerosol reflectance might exceed the LUT limits and produce SSA values above 1 or less than the maximum absorption in the LUT, typically referred to as out-of-bounds retrieval. We avoid this by constraining our inversion procedure within the LUT limits and do not allow for any extrapolation of the radiances. However, this leads to the unequal number of retrieved observations within and between the sensor wavelengths. In other words, for a given observation within the OMI or MODIS sensor, it is possible to have aerosol SSA retrieved at one wavelength and no retrieval (out-of-bounds) at other wavelengths.

To examine the spectral dependence of aerosol absorption, we created a subset of the data that includes observations for which aerosol SSA is retrieved for all the corresponding sensor wavelengths simultaneously (OMI: 340, 354, and 388 nm; MODIS: 466 and 646 nm) on any given day. This step reduces the sample size drastically but eliminates the need for making prior assumptions on the wavelength dependence of aerosol absorption to fill those gaps. The obtained subset of aerosol SSA in the UV–visible range is used to compute the resulting spectral dependence of aerosol absorption of the prevailing aerosols over the corresponding AERONET sites in terms of the aerosol absorption Ångström exponent (AAE), a measure of the spectral dependence of aerosol absorption optical depth (Bond, 2001) using a power-law approximation, analogous to the extinction Ångström exponent (van de Hulst, 1957). The spectral dependence of aerosol absorption AAE is defined as the slope of aerosol absorption optical depth with wavelengths on a log–log scale. The aerosol absorption optical depth $\tau_{abs}(\lambda)$ is derived as shown in Eq. (4):

$$\tau_{abs}(\lambda) = \left(1 - \omega_o(\lambda)\right) \cdot \tau_{ext}(\lambda), \quad (4)$$

from which the AAE for wavelength range λ_1, λ_2 is calculated as shown in Eq. (5).

$$\text{AAE}(\lambda_1, \lambda_2) = -\frac{\ln\left(\tau_{abs}(\lambda_1)/\tau_{abs}(\lambda_2)\right)}{\ln(\lambda_1/\lambda_2)} \quad (5)$$

The results presented hereafter include only a data subset that meets the following three conditions: (a) SSA retrievals are available for all five wavelengths on a given day, (b) $\tau_{440} > 0.4$ to ensure reliable accuracy spanning the UV–visible wavelengths, and (c) there are at least 5 d of observations available per season per aerosol type.

4 SSA retrieval sensitivity analysis

The proposed inversion procedure to derive spectral aerosol absorption from the combined ground and satellite measurements is susceptible to several systematic and random errors. These error sources include uncertainties in the following input parameters: (a) aerosol extinction measurements, (b) estimation of particle sizes (volume mean radius, VMR), (c) real part of the refractive index (RRI), (d) calibration of satellite-measured TOA radiances, (e) sub-pixel cloud contamination,

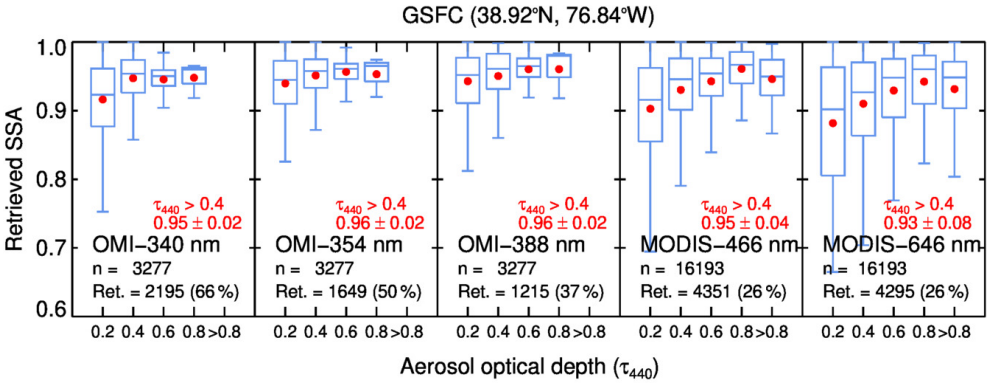

Figure 4. Retrieved aerosol SSA over the GSFC site for the satellite observation period of 2005–2016. Average and standard deviation of retrieved SSA for the observations with $\tau_{440} > 0.4$ are shown in red. n is the number of satellite–AERONET collocated observations and "ret." is the number of observations for which SSA is retrieved.

(f) O_3 and NO_2 gaseous absorption in the RTM, (g) surface reflectance, (h) ALH, (i) surface pressure, and (j) variability in AOD for the satellite observations within ±2 h and 50 km radius of the AERONET measurement. The retrieved aerosol absorption from our inversion procedure could be affected by all these sources of uncertainties. Errors associated with surface reflectance, ALH, and cloud contaminations on the satellite-retrieved optical depths are well documented in the literature (e.g., Fraser and Kaufman, 1985; Torres et al., 1998; Jethva et al., 2014). In summary, it is known that (i) an overestimation (underestimation) of surface reflectance leads to lower (higher) aerosol SSA, (ii) an overestimation (underestimation) of τ leads to lower (higher) aerosol SSA, (iii) an overestimation (underestimation) of ALH produces higher (lower) aerosol SSA (significantly more pronounced in the UV than in visible wavelengths), and (iv) an increase in TOA reflectance due to sub-pixel cloud contamination produces higher aerosol SSA.

4.1 Estimation of theoretical errors in the retrieved aerosol $\omega_o(\lambda)$

Here, we conduct sensitivity tests for all sources of errors in the input variables to derive a theoretical estimate of the error percolated in the aerosol SSA retrieval due to uncertainties in the assumed values of these variables. To have a controlled setup, we performed tests for a representative fixed satellite–sun geometry (SZA = 20°, VZA = 20°, RAA = 130°) over the GSFC, Mongu_Inn, and Tamanrasset_INM sites. These sites were selected to represent three distinct aerosol types as well as surface conditions. We assume a fixed value of $\omega_o = 0.9$ at 388 nm and aerosol load $\tau_{440} = 0.2$, 0.3, and 0.4 as our references to estimate errors in the retrieved SSA. To derive corresponding spectral AODs at remaining wavelengths, we assume an $EAE_{340-646}$ of 1.9, 0.2, and 1.9 for carbonaceous, dust, and urban aerosols, respectively. Similarly, spectral SSA at other wavelengths is estimated assuming an $AAE_{340-646}$ of 1.7, 2.5, and 0.9 for carbonaceous, dust, and urban aerosols, respectively. We calculate the uncertainty of the derived spectral SSA for each aerosol type by perturbing, one at a time, the nominal values of the nine inputs parameters by an assumed or observationally known uncertainty. The absolute error is computed as the SSA obtained with altered input minus the assumed SSA. The combined uncertainty of the derived spectral SSA is given by square root of the summation of the squares of the errors associated with each parameter.

4.1.1 Theoretical errors in retrieved ω_o (λ) due to τ_{ext}, VMR, and RRI

Figure 5 shows the error analysis of the retrieved SSA as a function of wavelength and optical depth given a change in the input (a) $\tau_{ext}(\lambda)$, (b) volume mean radius of the particles, and (c) real part of the refractive index. We perturb the input τ with an absolute value of ±0.02 for $\lambda < 400$ nm and ±0.01 for $\lambda > 400$ nm as prescribed by the AERONET AOD product. As shown in Fig. 5a, AOD overestimations result in SSA underestimations, whereas AOD underestimations yield SSA overestimations for all aerosol types over the considered spectral range. The magnitude of the SSA error ($\Delta\omega_o$) decreases with increasing AOD. It is noted that for all aerosol types with an underestimation (overestimation) of AOD, the magnitude of $\Delta\omega_o$ is positive (negative) and increases with wavelength (340–388 and 466–646 nm). The higher magnitudes of $\Delta\omega_o$ noted for visible wavelengths are attributed to lower spectral AODs where the aerosol absorption signal is diminished for a stable retrieval, particularly notable for weakly absorbing urban aerosols. For the reference $\tau_{440} = 0.4$, perturbation of $\pm 0.02 + \tau$ at 340 nm yields an error $\Delta\omega_o$ within ±0.002, while a perturbation of $\pm 0.01 + \tau$ at 646 nm yields an error within ±0.011.

Uncertainties in assumed particle sizes are also expected to affect the retrieval of aerosol absorption. To estimate the error incurred in our SSA retrieval, we perturb the particle volume mean radius derived from all AOD observations by

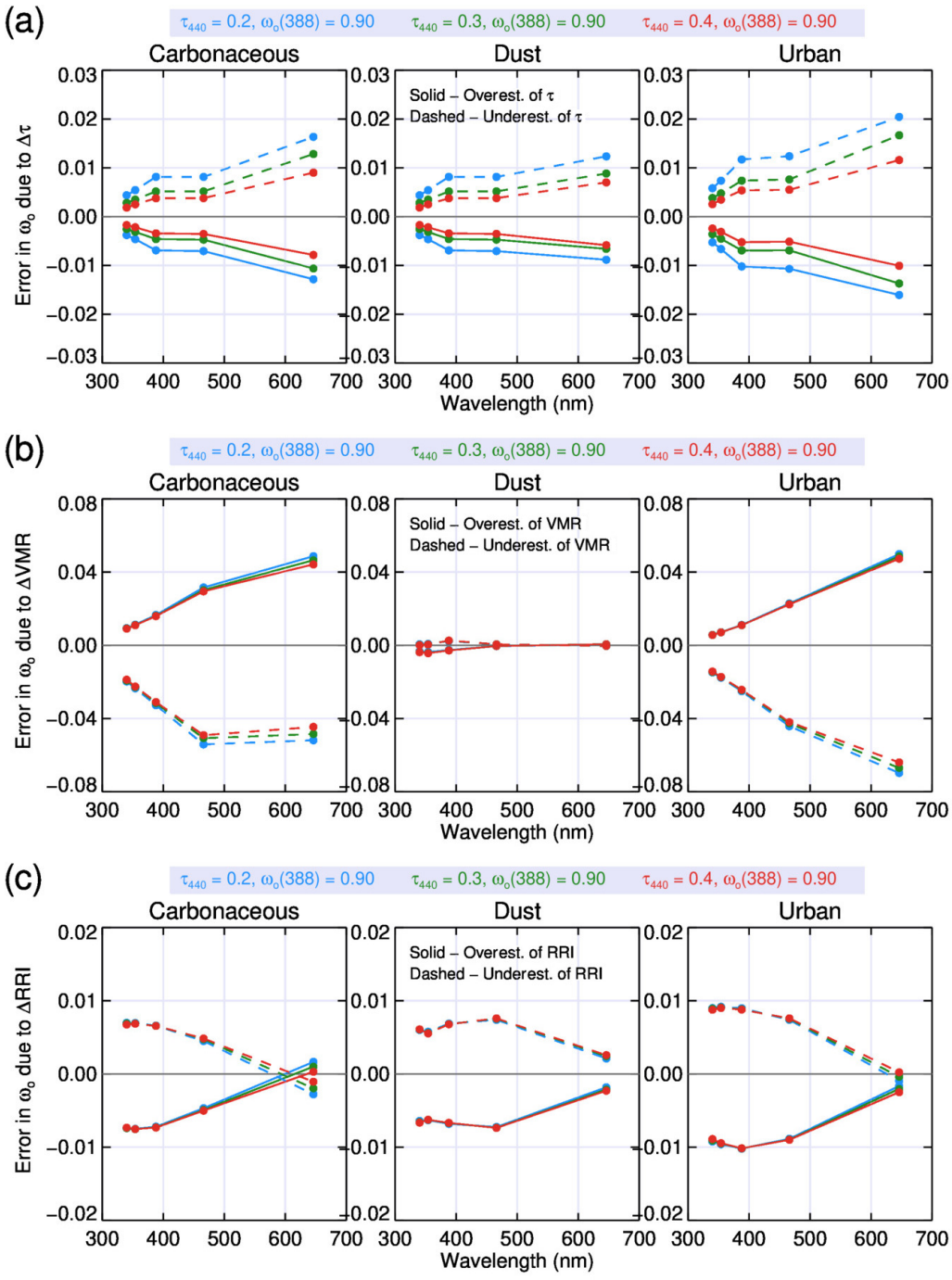

Figure 5. Theoretical uncertainty in SSA retrievals due to changes in **(a)** ±0.02 ($\lambda < 400$ nm) and ±0.01 ($\lambda > 400$ nm) τ, **(b)** ±20 % volume mean radius (VMR), and **(c)** ±0.04 real part of the refractive index (RRI). Solid and dashed lines represent the overestimation and underestimation of the corresponding input variable.

20 %. We chose $\Delta\mathrm{VMR} = 20\,\%$ based on examination of seasonal climatology of particle sizes as a function of τ_{440} and the most frequently occurring τ_{440} bin. It is noted that an overestimation of particle radii produces higher aerosol SSA, leading to positive $\Delta\omega_o$ and vice versa for carbonaceous and urban aerosols. Spectrally, the magnitude of $\Delta\omega_o$ is at a minimum in the UV and increases towards the visible wavelengths. The magnitude and spectral behavior of $\Delta\omega_o$ noted here suggests aerosol scattering primarily drives the particle size effect. For dust aerosols, the $\Delta\omega_o$ noted is quite small/negligible in UV wavelengths, while it remains invariant at the visible spectral range. This is due to the size of

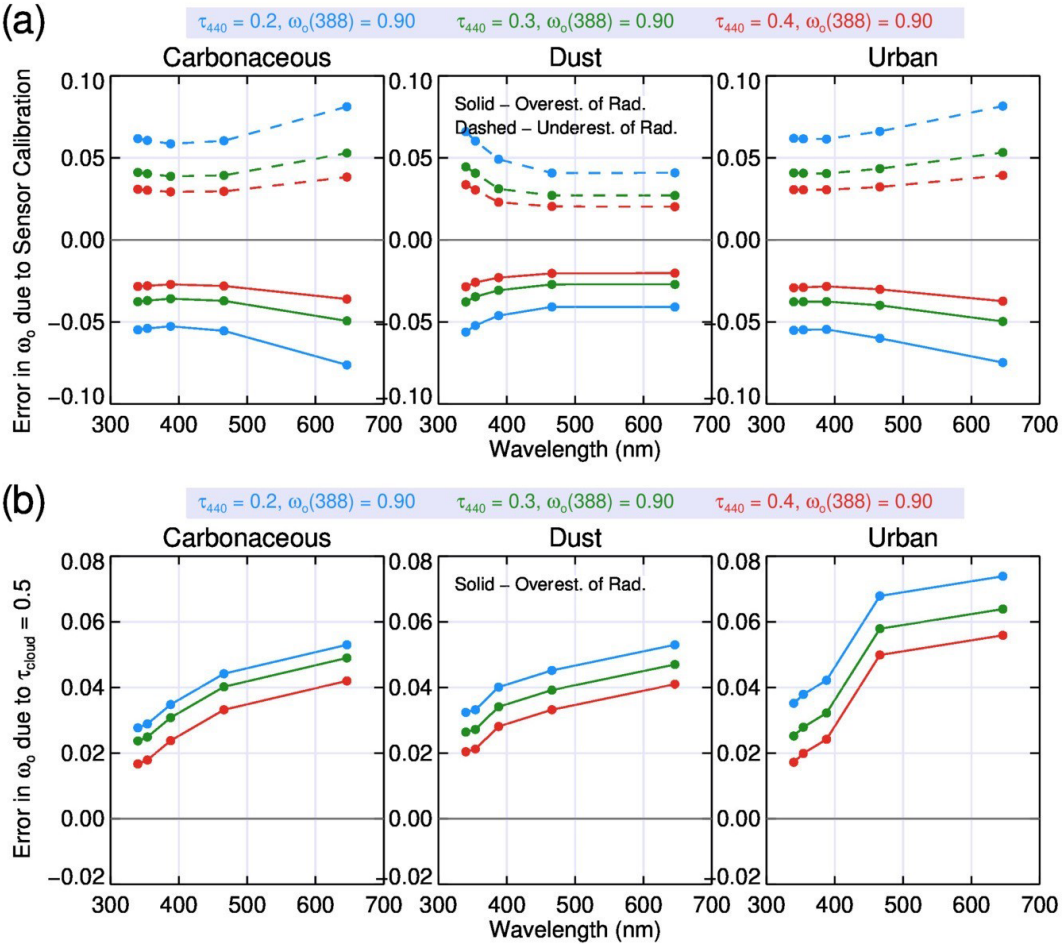

Figure 6. Theoretical uncertainty in SSA retrievals due to **(a)** ±1.8 % (OMI) and ±1.9 % (MODIS) sensor calibration and **(b)** cloud contamination ($\tau_{cloud} = 0.5$). Solid and dashed lines represent the overestimation and underestimation of the corresponding input variable.

dust particles that is much higher than the considered spectral range where extinction of radiation reaches maximum efficiency and remains less variant with an additional increase in particle sizes. It should be noted that at the AODs considered ($\tau_{440} = 0.2$, 0.3, and 0.4), particle size assumptions here have only a small effect on the retrieved SSA for all aerosol types. However, the increase in particles sizes due to processes such as coagulation and condensation at higher AOD levels might likely add additional errors in the estimated $\Delta\omega_o$. For the reference $\tau_{440} = 0.4$, a perturbation of ±20 % VMR in all aerosol types yields an error $\Delta\omega_o$ within ±0.018 and ±0.044 at 340 and 646 nm, respectively.

Another aerosol intrinsic property input for our SSA retrieval algorithm obtained from AERONET inversion product is the real part of the refractive index (RRI) – which primarily contributes to the magnitude of scattering. The prescribed uncertainty in aerosol RRI is estimated to be ±0.04 (Dubovik et al., 2000). Our results indicate that an overestimation of RRI produces lower aerosol SSA and vice versa. The effect of aerosol RRI perturbation on retrieved SSA is noted to be higher in the UV spectrum than in the visible. This is likely a result of strong competing effects from molecular scattering and aerosol absorption, while aerosol load adds an additional weak dependence. For the reference $\tau_{440} = 0.4$, perturbation of ±0.04 + RRI yields an error $\Delta\omega_o$ within ±0.009 and ±0.002 at 340 and 646 nm, respectively.

4.1.2 Theoretical errors in retrieved ω_o (λ) due to OMI/MODIS calibration and cloud contamination

Figure 6 shows the error analysis of the retrieved SSA as a function of wavelength and optical depth given a change in the (a) TOA radiances due to sensor calibration and (b) subpixel cloud contamination. The prescribed uncertainty in the TOA radiance measurements for OMI and MODIS sensors is expected to be ±1.8 % (Schenkeveld et al., 2017) and ±1.9 % (Guenther et al., 2002; Xiong et al., 2018), respectively. As expected, an overestimation of TOA radiances due to sensor calibration produces lower aerosol SSA and vice

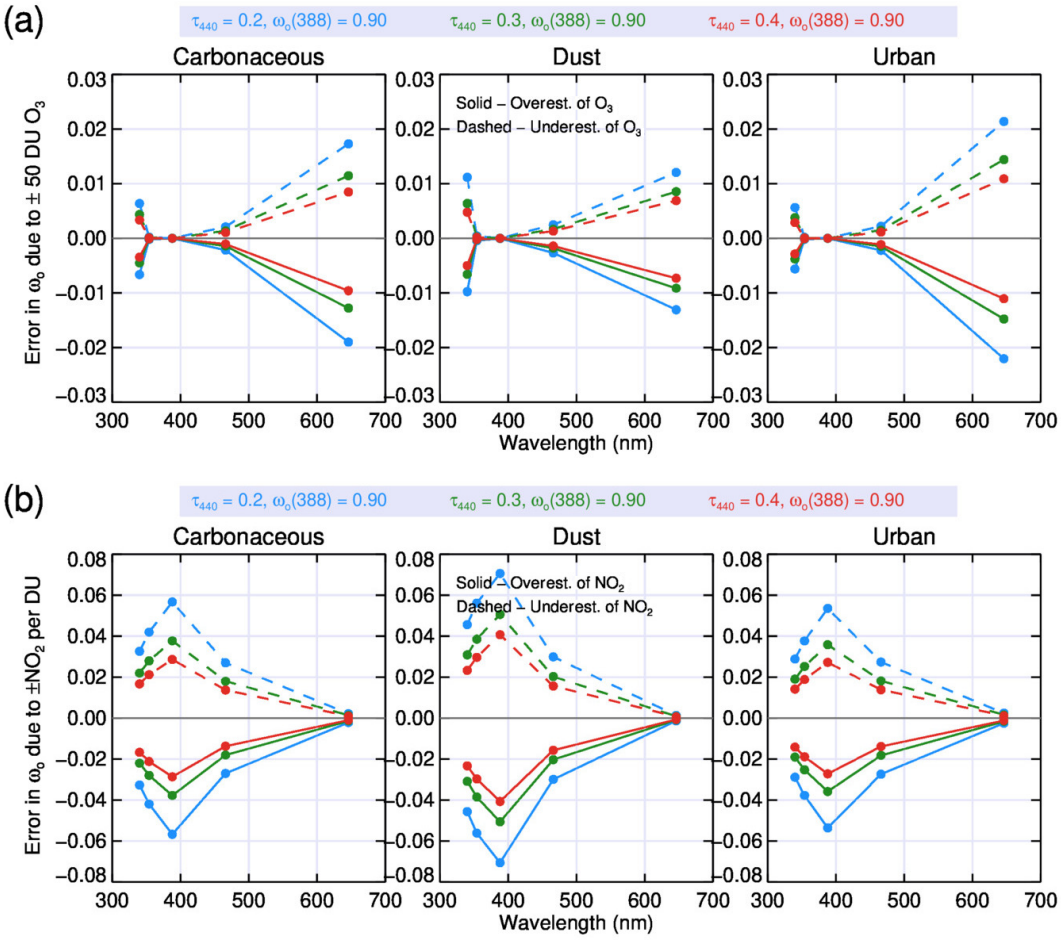

Figure 7. Theoretical uncertainty in SSA retrievals due to **(a)** ±50 DU O_3 and **(b)** ±1 DU NO_2 concentrations. Solid and dashed lines represent the overestimation and underestimation of the corresponding input variable.

versa. Errors in the retrieved SSA due to uncertainties in the sensor calibration increase with decreasing aerosol optical depth. For the reference $\tau_{440} = 0.4$, perturbation of ±1.8 % in TOA radiances at 340 nm yields an error $\Delta\omega_o$ within ±0.027, while a perturbation of ±1.9 % in TOA radiances at 646 nm yields an error within ±0.037. To estimate the error incurred in the retrieval of aerosol SSA due to cloud contamination, we developed LUTs for each aerosol type assuming a cloud of optical thickness 0.5 in our RT simulations. These LUTs are used to compute the sensitivity of aerosol SSA due to the presence of an optically thin cloud layer in the atmosphere. Our results demonstrate that the assumed optically thin cloud ($\tau_{cloud} = 0.5$) produces an overestimation of TOA radiances, leading to higher aerosol SSA. The effect of cloud contamination in TOA radiances is more pronounced in the visible than in UV spectrum. For observations with $\tau_{440} = 0.4$, the cloud contamination yields an error $\Delta\omega_o$ within ±0.020 and ±0.056 at 340 and 646 nm, respectively.

4.1.3 Theoretical errors in retrieved ω_o (λ) due to O_3 and NO_2 gaseous absorption

As described in Sect. 1, for the retrieval of aerosol properties from satellite-measured radiances it is important to separate the TOA radiance signal from the underlying surface and atmospheric constituents including trace gases. It should be noted that the RTM used in this work accounts only for the H_2O and O_3 gaseous absorption. In addition, we applied a correction for the retrieved aerosol SSA to account for NO_2 absorption. Here we estimate the error incurred in our aerosol SSA retrievals due to uncertainties in the employed O_3 and NO_2 amounts available through the AERONET AOD product. Based on the variability of O_3 and NO_2 columnar amounts and their uncertainties (not shown here) for the sites used in this work, a perturbation of ±50 and ±1 DU for O_3 and NO_2 respectively is chosen to estimate the error incurred in our retrievals. Our results, as shown in Fig. 7, indicate that overestimation of O_3 amounts by +50 DU produces lower SSA (higher absorption), leading to negative $\Delta\omega_o$, while underestimation of O_3 amounts produces higher

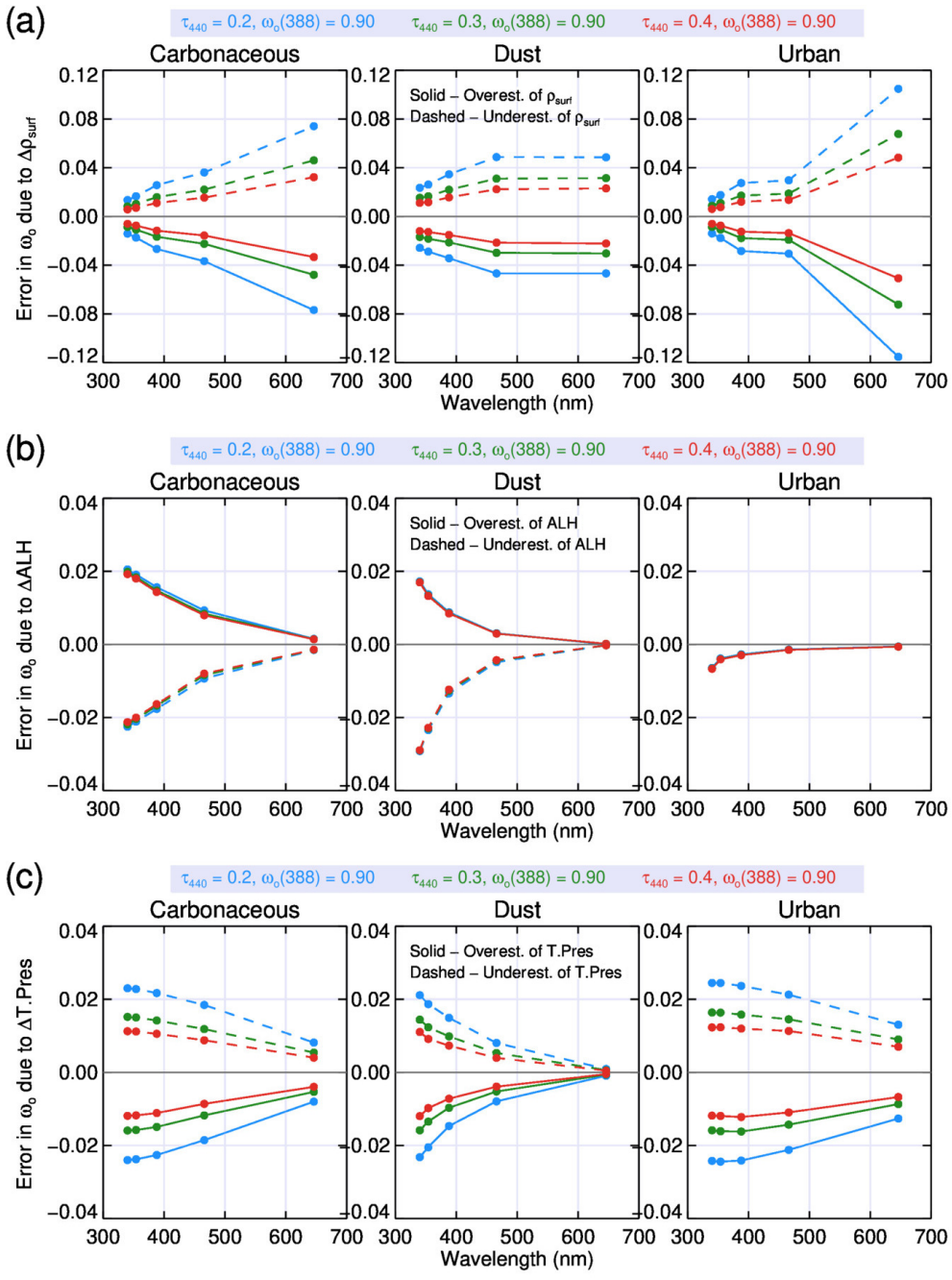

Figure 8. Theoretical uncertainty in SSA retrievals due to changes in **(a)** ±0.01 surface reflectance, **(b)** ±1 km ALH, and **(c)** ±12 hPa surface pressure. Solid and dashed lines represent the overestimation and underestimation of the corresponding input variable.

SSA (lower absorption), leading to positive $\Delta\omega_o$. Similar to O_3 amounts, an overestimation of NO_2 amounts produces lower SSA, yielding negative $\Delta\omega_o$ and vice versa. The error in retrieved SSA due to ±50 DU of O_3 is noted to be within 0.008 at 340 nm and increases towards the visible spectrum at 646 nm ranging 0.009–0.018 for observations with τ_{440} up to 0.4. However, the error in retrieved SSA due to underestimation of NO_2 per DU perturbation increases from 0.023 to 0.040 at 340 to 388 nm and decreases towards the visible wavelengths to 0.018 and 0.001 at 466 and 646 nm, respectively, for $\tau_{440} = 0.4$. The spectral curvature of $\Delta\omega_o$ due to O_3 and NO_2 amounts is consistent with the known spectral absorption behavior of O_3 and NO_2. In addition, as expected the error in $\Delta\omega_o$ for both O_3 and NO_2 perturbation increases with a decrease in τ_{440}. For observations with $\tau_{440} = 0.4$, a perturbation of ±50 DU of O_3 amount yields an error $\Delta\omega_o$

within ±0.005 and ±0.011 at 340 and 646 nm, respectively, while a perturbation of ±1 DU of NO_2 amount yields an error $\Delta\omega_o$ within ±0.023 and ±0.001 at 340 and 646 nm respectively.

4.1.4 Theoretical errors in retrieved ω_o (λ) due to surface reflectance, ALH, and surface pressure

Figure 8 shows the error analysis of the retrieved SSA as a function of wavelength and optical depth given a change in the (a) surface reflectance, (b) ALH, and (c) surface pressure. We perturb the surface reflectance by an absolute ±0.01 for all wavelengths to derive an estimate of error incurred in the SSA retrieval. Our results indicate that $\Delta\omega_o$ increases with increasing wavelength and decreasing τ due to changes in surface reflectance for all aerosol types. For less-absorbing (urban) aerosols, the surface reflectance becomes increasingly important at the visible wavelengths than compared to absorbing (carbonaceous or dust) aerosols. For the observations with $\tau_{440} = 0.4$, it is noted that $\Delta\omega_o$ values are within ±0.011 and ±0.050 at 340 and 646 nm, respectively. In contrast to the surface reflectance, the effect of ALH becomes prominent at near-UV wavelengths under the prescribed uncertainty of ±1 km. The $\Delta\omega_o$ due to changes in ALH decreases with wavelength because of the gradually diminishing intensity of Rayleigh scattering (proportional to λ^{-4}) and its radiative interactions with aerosols. For the observations with $\tau_{440} = 0.4$, it is noted that $\Delta\omega_o$ values due to ±1 km ALH are within ±0.028 and ±0.001 at 340 and 646 nm respectively for both absorbing and non-absorbing aerosols.

Another essential input in our SSA retrieval algorithm employed here is the terrain or surface pressure that determines the contribution of molecular scattering in the simulated TOA radiances through pre-computed LUT. We assume an uncertainty of ±100 m in the terrain height equivalent to ±12 mbar or hPa pressure to derive an estimate of error incurred in aerosol SSA. Our analysis indicates that an overestimation of surface pressure produces lower aerosol SSA to compensate for the higher radiances reaching the TOA. For absorbing (carbonaceous or dust) aerosols, the effect of surface pressure on the retrieved SSA is higher in the UV spectrum than in the visible spectrum, while for less-absorbing (urban) aerosols the errors in retrieved SSA in the UV and visible spectral range are comparable, exhibiting a relatively small slope. Colarco et al. (2017) provide a detailed examination of the effect of terrain pressure on OMI measurements and reported that these effects are prominent at sites over mountainous regions owing to the coarser OMI footprint. In addition to the surface elevation uncertainty, their study investigates the differences in OMAERUV (static) and MERRA (6-hourly) surface pressure and reports differences up to ±15 hPa over land and higher over oceans. Therefore, the assumed uncertainty of ±100 m terrain height (∼ ±12 hPa) in our sensitivity test accounts well for both of these effects. For the observations with $\tau_{440} = 0.4$, it is noted that $\Delta\omega_o$ due to ±12 hPa surface pressure is within ±0.011 and ±0.006 at 340 and 646 nm, respectively.

4.1.5 Theoretical errors in retrieved ω_o (λ) due to variability in AOD around the site

The final variable that could possibly incur error in our SSA retrievals is the point AOD measurement from AERONET that is assumed homogenous/constant for the satellite radiance measurements within ±2 h and 50 km radius of the site. To estimate the error in our retrieved SSA due to this assumption we initially estimate the variability in AOD derived from OMAERUV and MODIS-DB AOD products, as well as ±2 h of AERONET AOD from the satellite overpass times. Based on the variability of AOD (not shown here) for the pixels within ±2 h and 50 km radius of all sites considered, we use a perturbation of ±0.2 for $\lambda < 400$ nm and ±0.1 for $\lambda > 400$ nm to determine the error in our SSA retrievals. As demonstrated previously, an overestimation of AOD produces lower SSA (negative $\Delta\omega_o$) and vice versa. For the observations with $\tau_{440} = 0.4$, it is noted that $\Delta\omega_o$ due to ±0.2 perturbation to the measured τ is within ±0.022 at 340 nm and that due to ±0.1 perturbation is within 0.053 at 646 nm, respectively.

4.1.6 Combined maximum theoretical errors in retrieved ω_o (λ) due to all input variables

Table 2 summarizes the SSA error analysis at 340 and 646 nm due to uncertainties in most relevant input variables. Among all input variables used in our algorithm, the $\Delta\omega_o$ at 340 nm arises mostly from (in descending order) the uncertainties in calibration of TOA radiances, spatiotemporal variability in the assumed homogeneous AOD over the site, sub-pixel cloud contamination, ALH, particle sizes, and so on, whereas for the visible wavelength at 646 nm the $\Delta\omega_o$ arises mostly from (in descending order) cloud contamination, surface reflectance, calibration of TOA radiances, particle sizes, trace gases, and so on. These sensitivity tests clearly indicate that $\Delta\omega_o$ (a) is spectrally dependent due to multiple variables, (b) decreases with increasing τ, and (c) varies with absorbing nature of aerosols. The combined error in retrieved SSA can now be estimated as the square root of the sum of individual error squares (RMSE). Overall, for the observations with $\tau_{440} = 0.4$, the combined error in the retrieved SSA for absorbing (less-absorbing) aerosols is within ±0.051 (±0.043) and ±0.073 (±0.108) at 340 and 646 nm, respectively. However, it should be noted that depending on the reliability of the input variables, the errors stemming from individual sources could be in the opposite direction, resulting in the cancellation of errors. Under such scenario, the combined error in the retrieved spectral SSA is expected to be much lower than the maximum combined value reported here with our sensitivity tests.

Table 2. Theoretical estimated uncertainties in the retrieval of aerosol SSA due to error in the input variables. The configuration of sensitivity tests is as follows: SZA = 20°, VZA = 40°, RAA = 130°, and $\omega_o(388) = 0.9$.

	Input uncertainty	Theoretical SSA uncertainty ($\Delta\omega_o$) for $\tau_{440} = 0.4$					
		$\lambda = 340$ nm			$\lambda = 646$ nm		
		Carb.	Dust	Urban	Carb.	Dust	Urban
Extinction AOD	$\lambda < 400$ nm, $\Delta\tau = \pm 0.02$ $\lambda > 400$ nm, $\Delta\tau = \pm 0.01$	0.002	0.001	0.002	0.009	0.007	0.011
Particle sizes	ΔVMR = ±20 %	0.018	0.003	0.014	0.044	0.0006	0.040
Real part of the refractive index	ΔRRI = ±0.04	0.007	0.007	0.009	0.001	0.002	0.002
Calibration of TOA measurements	OMI = ±1.8 % MODIS = ±1.9 %	0.026	0.021	0.027	0.020	0.027	0.037
Surface reflectance	$\Delta\rho_{surf} = \pm 0.01$	0.006	0.011	0.006	0.032	0.022	0.050
Aerosol layer height	ΔALH = ±1 km	0.021	0.028	0.006	0.001	0.001	0.0006
Presence of cloud	$\tau_{cloud} = 0.5$	0.016	0.020	0.017	0.042	0.041	0.056
Surface pressure	±12 mbar/hPa	0.011	0.011	0.011	0.004	0.0004	0.006
Variability in AOD	$\lambda < 400$ nm, $\Delta\tau = \pm 0.2$ $\lambda > 400$ nm, $\Delta\tau = \pm 0.1$	0.022	0.014	0.012	0.006	0.001	0.053
O_3 absorption	±50 DU	0.003	0.005	0.003	0.008	0.007	0.011
NO_2 absorption	±1 DU	0.016	0.023	0.014	0.001	0.0007	0.001
Max. combined theoretical uncertainty		0.051	0.047	0.043	0.073	0.055	0.108

4.2 Estimation of theoretical errors in the derived AAE

Similar to the estimation of errors in the retrieval of SSA, we conduct sensitivity tests to determine the errors in the computed AAE due to certainties in the retrieved SSA. We assume a fixed $\omega_o(388)$ of 0.9, an aerosol load τ_{440} of 0.4, and $EAE_{340-646}$ values of 1.9, 0.2, and 1.9 for carbonaceous, dust, and urban aerosols, respectively, to derive the nominal AAE values at three wavelength pairs: 354–388, 466–646, and 340–646. By using fixed $\tau(\lambda)$, we perturb the $\omega_o(\lambda)$ by ±0.01 intervals to compute the AAE. The uncertainty assumed here for the $\omega_o(\lambda)$ includes errors due to all variables as described in the above section. The errors are reported as difference in AAE from perturbed SSA minus the AAE derived from nominal SSA.

Table 3 presents the theoretical uncertainty in computed AAE due to uncertainties in the SSA. As expected, the ΔAAE noted for all wavelength pairs increases with increasing $\Delta\omega_o$ for all aerosol types. It is noted that for fine-mode particles (carbonaceous and urban), an overestimation of ω_o produces lower AAE (negative errors) and an underestimation of ω_o produces higher AAE (positive errors). In contrast, for coarse-mode particles, an overestimation of ω_o produces higher AAE (positive errors) and an underestimation of ω_o produces lower AAE (negative errors). This is due to the fact that large particle size drives the scattering effect, producing low aerosol absorption optical depths, and, therefore, further overestimation of ω_o yields lower single scattering co-albedo ($1 - \omega_o$). The magnitude of ΔAAE is higher for overestimation than that noted for underestimation of SSA. In addition, it is noted that for fine-mode particles the errors in $\Delta AAE_{354-388}$ (UV spectral range) are higher, while for coarse-mode particles the errors in $\Delta AAE_{466-646}$ (visible spectral range) are higher than the other two wavelength pairs. For the assumed carbonaceous aerosols, perturbation of $\Delta\omega_o = \pm 0.04$ yields a ΔAAE within ±0.13 for all wavelength pairs. For the urban aerosols, perturbation of $\Delta\omega_o = \pm 0.04$ yields a ΔAAE within ±0.70 for all wavelength pairs. However, for dust a perturbation of $\Delta\omega_o = \pm 0.04$ yields a ΔAAE up to ±1.3 for the 354–388 wavelength pair and much higher in the 466–646 and 340–646 wavelength pairs. Additional tests were performed by perturbing only one of the SSA values while deriving AAE for any wavelength pair. The resulting ΔAAE is much higher than for the tests where SSA is perturbed for all wavelengths. It is noted that for even a small perturbation of $\Delta\omega_o = \pm 0.01$ at one of the wavelengths in a pair, the ΔAAE is ±1.2, ±0.2, and ±0.4 for the wavelength pairs at 354–388, 466–646, and 340–646 respectively for all aerosol types. Overall, the errors noted for AAE are consistent with the wavelength dependence of ω_o that is a function of both size and absorbing nature of the particles.

Table 3. Theoretical uncertainties in the computation of absorption Ångström exponent.

		$\Delta\omega_o$	ω_o overestimation			ω_o underestimation		
			$\Delta AAE_{354-388}$	$\Delta AAE_{466-646}$	$\Delta AAE_{340-646}$	$\Delta AAE_{354-388}$	$\Delta AAE_{466-646}$	$\Delta AAE_{340-646}$
Carbon.	$\tau_{440} = 0.4$	0.01	−0.022	−0.021	−0.021	0.018	0.017	0.018
	$EAE_{340-646} = 1.9$	0.02	−0.051	−0.046	−0.048	0.034	0.031	0.032
	$\omega_o(388) = 0.90$	0.03	−0.087	−0.078	−0.081	0.046	0.044	0.045
	$AAE_{340-646} = 1.7$	0.04	−0.135	−0.119	−0.126	0.058	0.054	0.056
Dust	$\tau_{440} = 0.4$	0.01	0.228	0.688	0.488	−0.190	−0.423	−0.325
	$EAE_{340-646} = 0.2$	0.02	0.506	2.067	1.369	−0.351	−0.711	−0.562
	$\omega_o(388) = 0.90$	0.03	0.854	8.769	5.024	−0.489	−0.922	−0.744
	$AAE_{340-646} = 2.5$	0.04	1.302	–	–	−0.609	−1.082	−0.889
Urban	$\tau_{440} = 0.4$	0.01	−0.117	−0.077	−0.092	0.095	0.066	0.077
	$EAE_{340-646} = 1.9$	0.02	−0.265	−0.166	−0.204	0.173	0.124	0.144
	$\omega_o(388) = 0.90$	0.03	−0.458	−0.272	−0.343	0.239	0.175	0.201
	$AAE_{340-646} = 0.9$	0.04	−0.722	−0.399	−0.522	0.295	0.221	0.250

5 Comparison with AERONET SSA product

We compare our aerosol SSA retrievals at visible wavelengths with those from the AERONET inversion data set. The comparison is limited to AERONET level 2 reliable retrievals as determined the aerosol load at 440 nm ($\tau_{440} > 0.4$). We emphasize here that since AERONET SSA is a derived quantity and cannot be considered as ground truth, this comparison serves as a consistency check rather than a strict validation exercise. The nearest AERONET wavelength available for comparison with OMI wavelength (388 nm) retrievals is at 440 nm. To facilitate the comparison, we use the AAE computed from our retrievals at the 388–466 wavelength pair to transform the retrieved SSA at 388 to 440 nm (440_{OMI}). While at the MODIS wavelengths 466 and 646 nm, the AERONET SSA values were computed by linear interpolation of the values reported at 440 and 675 nm. This conversion is unlikely to introduce notable bias in our comparison as the difference in the nearest wavelengths of both data sets is very low (< 30 nm).

First, we investigate the consistency of retrieved SSA for selected sites for which the prevailing aerosol types and local source environment are well known as documented in several studies in the literature. We use the AERONET SSA from the period 2005–2016 for the comparison. Figure 9 shows the comparison of spectral SSA (boxplots showing lower and upper quartile of observations with the white line representing its mean value) for three distinct aerosol types sampled from the selected sites. The mean AAE derived for the visible wavelength pair at 466–646 nm agrees within 0.5 or less with the AERONET values for all aerosol types and sites considered. However, it should be noted that AAE is highly susceptible to small changes in the retrieved SSA for both data sets. For dust aerosols, the retrieved average SSA values show good agreement with AERONET SSA obtained at Dakar and Ouagadougou (within ±0.008), while the differences in SSA (retrieved minus AERONET) at Tamanrasset and Solar Village are 0.02 and 0.05, respectively, at 466 nm. Although our sample is limited to the few days that met our criteria for the subset, the observed differences in SSA are within the overall uncertainty estimates presented in the previous section. For carbonaceous particles, the retrieved and AERONET SSA agree well with differences of less than 0.015 for Alta Floresta, Cuiabá, and Mongu. However, a notable difference in SSA (0.045) is observed at Lake Argyle, with higher absorption for AERONET than our retrieved value at both 466 and 646 nm. For urban/industrial aerosols at GSFC, Avignon, Moldova, and Cairo, the retrieved SSA values agree within the uncertainty estimates. A particularly notable difference (−0.05) is found for Avignon at 646 nm. It should be noted that, while AERONET version 3 employs surface reflectance using bidirectional reflectance distribution function (BRDF) parameters from MODIS BRDF/Albedo CMG Gap-Filled Snow-Free Product MCD43GF (Sinyuk et al., 2020), we use the MODIS MCD19A1 BRF/surface reflectance product. The use of different surface reflectance data in the two retrieval algorithms likely contributes to some of the observed SSA differences. Although for AERONET SSA retrievals that use upward-viewing sky radiance measurements surface reflectance is a relatively small source of error, for our retrievals (as discussed in the sensitivity analysis) surface reflectance is the second-highest source of errors at visible wavelengths after cloud contamination. Additionally, for our retrievals as well as with AERONET, uncertainties in SSA increase with wavelength for fine-mode particles (carbonaceous and urban) with high EAE, notably for weakly

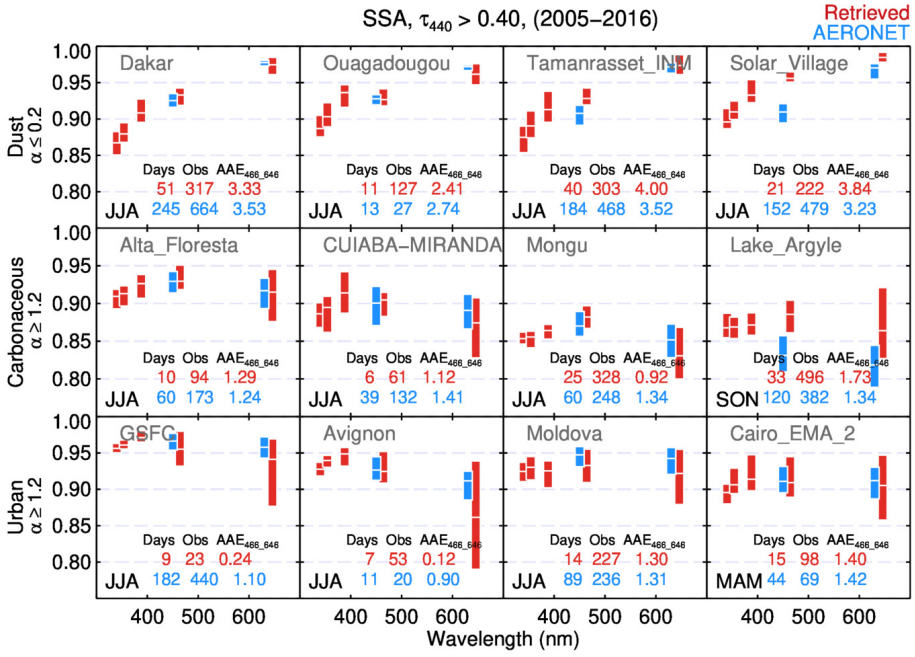

Figure 9. Comparison of retrieved aerosol SSA with that of AERONET for selected sites. Boxplots here represent lower and upper quartile of observations with mean values shown as the white line.

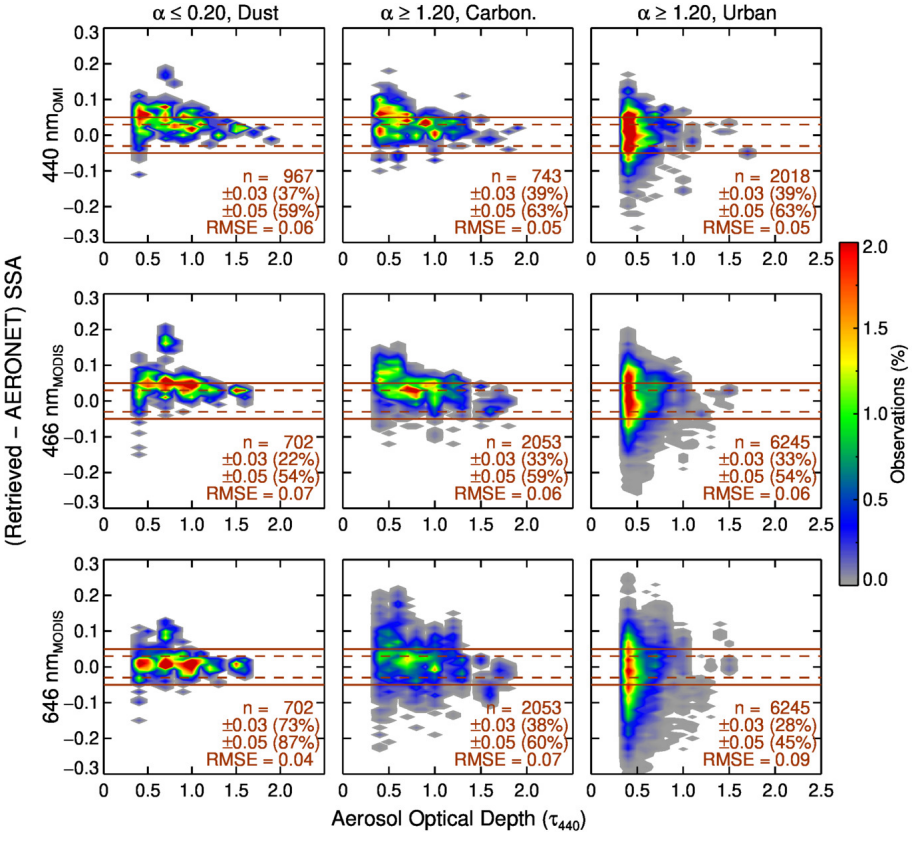

Figure 10. Absolute difference in retrieved minus AERONET SSA versus AOD for all observations with $\tau_{440} > 0.4$ for coarse-mode dust, fine-mode carbonaceous, and fine-mode urban aerosols at 440, 466, and 646 nm.

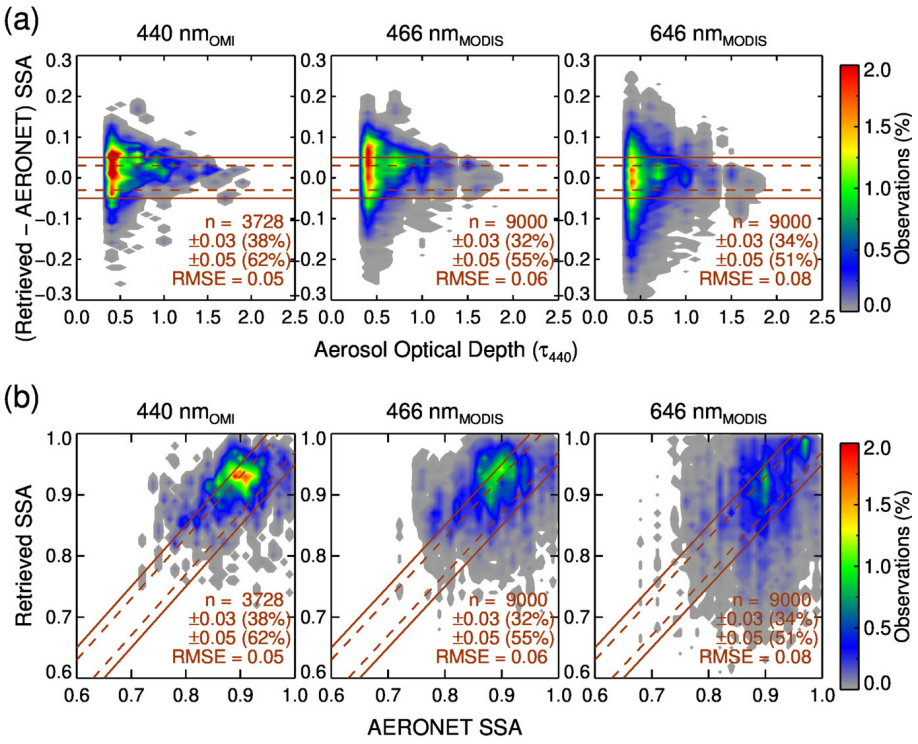

Figure 11. **(a)** Absolute difference in retrieved minus AERONET SSA versus τ_{440} and **(b)** retrieved SSA versus AERONET SSA for observations with $\tau_{440} > 0.4$ for the combined aerosol types at 440, 466, and 646 nm.

absorbing aerosols. For example, the ±0.03 uncertainty in AERONET SSA at 440 nm for $\tau_{440} \sim 0.4$ is achieved for the NIR wavelength (1020 nm) at $\tau_{440} \sim 0.6$ for the fine-mode particles observed over the GSFC site (Sinyuk et al., 2020).

Figure 10 shows the absolute difference in retrieved SSA with AERONET as a function of τ_{440} for all collocated observations. For the SSA at 440 nm$_{OMI}$, the observations within ±0.03 (±0.05) envelopes are 37 % (59 %), 39 % (63 %), and 39 % (63 %) for dust, carbonaceous, and urban aerosol types, respectively. As expected, the SSA difference is highest for lower AODs and decreases with increasing aerosol load for all aerosol types. For the SSA at 466 nm, the observations within ±0.03 (±0.05) envelopes are 22 % (54 %), 33 % (59 %), and 33 % (54 %) for dust, carbonaceous, and urban aerosol types, respectively. In terms of particle sizes, the difference in SSA for fine-mode particles ($\alpha_{440-870} > 1.2$) is noted to be more scattered than the difference in SSA noted for coarse-mode particles. This could be partially explained by the variability in sizes for fine-mode particles from the seasonal climatology of particle sizes employed in our algorithm. For the SSA at 646 nm, the observations within ±0.03 (±0.05) envelopes are 73 % (87 %), 38 % (60 %), and 28 % (45 %) for dust, carbonaceous, and urban aerosol types, respectively. Spectrally, there is significantly more scatter at 646 nm with SSA differences in the range −0.3 to 0.2 for urban aerosols. The RMSE of the SSA ranges from 0.04 to 0.09, with the lowest error for dust particles at 646 nm and the highest error for urban aerosols at the same wavelength. This is due to the high spectral AODs for coarse-mode particles through the UV–visible spectrum where sufficient absorption signal is available for the retrieval of SSA, whereas for fine-mode particles with the decreasing spectral AODs from the UV–visible spectrum the absorption signal becomes weak, which is particularly notable for the less absorbing (urban) aerosols.

Figure 11a shows the absolute difference in retrieved and AERONET SSA as a function of optical depth by combining all aerosol types together. The differences in SSA for all wavelengths at 440$_{OMI}$ and 466 and 646 nm are higher for lower τ and become negligible for higher τ. It is observed that at 440$_{OMI}$ and 466 nm the observations with positive differences are relatively higher than that at 646 nm. Comparison of the retrieved SSA with AERONET SSA for all aerosol types is shown in Fig. 11b. Our retrieved SSA at 440$_{OMI}$ and 466 and 646 nm agrees within ±0.03 of the AERONET SSA for 38 % (0.05), 32 % (0.06), and 34 % (0.08) of observations (RMSE) respectively.

It is important to note here that our retrieval method and that used in the AERONET inversion differ fundamentally in several aspects: (i) different source of surface reflectance data used; (ii) instantaneous particle sizes derived from sky radiance measurements by AERONET and seasonal climatological average particle sizes used in our retrievals; (iii) the use of multi-spectral, multi-angular sky radiance measure-

ments by AERONET along the almucantar plane or hybrid scan and the single-view TOA radiance measurements by the satellites in our retrievals; and (iv) the use of a relatively strong constraint on the spectral variation of the imaginary refractive index for the fine-mode particles in AERONET SSA retrievals, while our retrievals of SSA are carried for each wavelength independently. The use of a relatively strong constraint on the spectral variation of the imaginary refractive index for the fine-mode particles with high $\alpha_{440-870}$ for AERONET inversion is due to the lower spectral AODs and diminished absorption signal strength at higher wavelengths, which is insufficient for a robust absorption retrieval (Dubovik et al., 2006). The differences noted between our SSA retrievals and that from AERONET at different wavelengths could stem from one or more sources of the differences listed above.

6 Spectral aerosol absorption in major aerosol environments

In this section, we describe regional average aerosol absorption and AAE derived from our subset of results over worldwide regions dominated by carbonaceous, dust, and urban aerosols. The AERONET sites selected for this analysis are based on the dominant samples observed here and well-known aerosol sources from the literature (e.g., Eck et al., 2010, 2013; Giles et al., 2012, and references therein). The aerosol-typing scheme employed in this work based on UVAI and $\alpha_{440-870}$ is only to guide our algorithm to include ALH in the SSA retrieval procedure. Therefore, it should be noted that aerosol types as described below do not represent a robust characterization, and an overlap of aerosol samples is observed at few sites, especially over the regions where mixtures of aerosols are found.

The averages of aerosol SSA and AAE derived for all sites considered in this work are presented in Table S1 in the Supplement. In addition, the corresponding particle size distributions used for developing the LUT radiances for these sites are presented in the Supplement as well.

6.1 Carbonaceous aerosols

Emissions from biomass burning are one of the major contributors of carbonaceous aerosols found in the atmosphere. These carbonaceous aerosols are primarily composed of black carbon and organic carbon components in addition to minor fractions of inorganic components (Andreae and Merlet, 2001). Studies show that black carbon amounts in the atmosphere are high absorbers of solar radiation and have near-unity AAE due to the invariant imaginary part of the refractive index in the UV–visible spectrum (Bergstrom, 1973; Bohren and Huffman, 1983; Bergstrom et al., 2002). The typical spectral behavior for carbonaceous aerosols has decreasing SSA with increasing wavelength in the visible spectrum (Eck et al., 1998; Reid and Hobbs, 1998). Additionally, the presence of organic carbon amounts shows enhanced absorption in the UV region (Kirchstetter et al., 2004). Our observations for the carbonaceous aerosols from worldwide biomass burning regions depict these characteristics very well. The seasonal averages of spectral SSA for carbonaceous aerosols found over major aerosol environments are shown in Fig. 12.

For the Missoula site located in the northwestern United States (US), carbonaceous aerosols are observed during JJA in our sample. Aerosols observed over Missoula are primarily emitted from natural forest fires of the northwestern US in the dry season (June through September). The spectral SSA of these aerosols is noted to increase from 340 nm (0.89 ± 0.02) to 466 nm (0.94 ± 0.03) followed by a decrease toward the 646 nm (0.90 ± 0.06). Average τ_{440} and $\alpha_{440-870}$ are about 1.2 and 1.8 respectively, while the average $AAE_{340-646}$ is noted as 1.8. Our results are consistent with the in situ measurements of wildfire smoke at the Missoula ground station for the 2017 and 2018 summer, which reports an average SSA of 0.93–0.94 at 401 nm and AAE 1.7–1.9 over the spectral range 401–870 nm (Selimovic et al., 2020).

Over South America, our subset of carbonaceous aerosols is observed for sites at the Alta Floresta, Cuiabá, and Ji-Paraná in Brazil and the Santa Cruz site in Bolivia. In general, carbonaceous aerosols over South America are dominantly emitted from biomass burning during Southern Hemisphere spring (JJA) and summer (SON), with distinct peaks in August and September. Most aerosol emissions are associated with biomass burning for land and agricultural management practices. The regional average SSA of these aerosols at 466 nm is noted to be 0.92 ± 0.03 (0.93 ± 0.02) during JJA (SON) months. Spectral SSA increases from 0.90 ± 0.02 at 340 nm to 0.93 ± 0.03 at 388 nm followed by a decrease toward the visible wavelengths. Average τ_{440} and $\alpha_{440-870}$ are about 1 and 1.8 respectively, with mean $AAE_{340-646}$ ranging between 1.5–1.8 for both JJA and SON months. Among the sites considered here, the CUIABA-MIRANDA site located in the Cerrado ecosystem exhibits the highest aerosol absorption ($\omega_o \sim 0.90 \pm 0.03$ at 466 nm), while the remaining sites are surrounded by tropical rainforest and exhibit relatively less absorption ($\omega_o \sim 0.93 \pm 0.03$ at 466 nm). Burning of Cerrado (wooded savanna) and rainforest dominantly happens through the flaming and smoldering phase combustion respectively, resulting in the noted variation of aerosol absorption over these sites (Schafer et al., 2008).

Over southern Africa, our subset of carbonaceous aerosols is observed for sites at Mongu in Zambia and Skukuza in South Africa. Emissions from biomass burning primarily for agricultural and land management practices are a major source of aerosols over southern Africa (Eck et al., 2001, 2003). In addition, crop residue burning, heavy industrial facilities, and episodic dust commonly dictate the aerosol amounts over southern Africa. Fine-mode carbonaceous aerosols noted over these sites show high average absorption during the JJA period. The average SSA for these

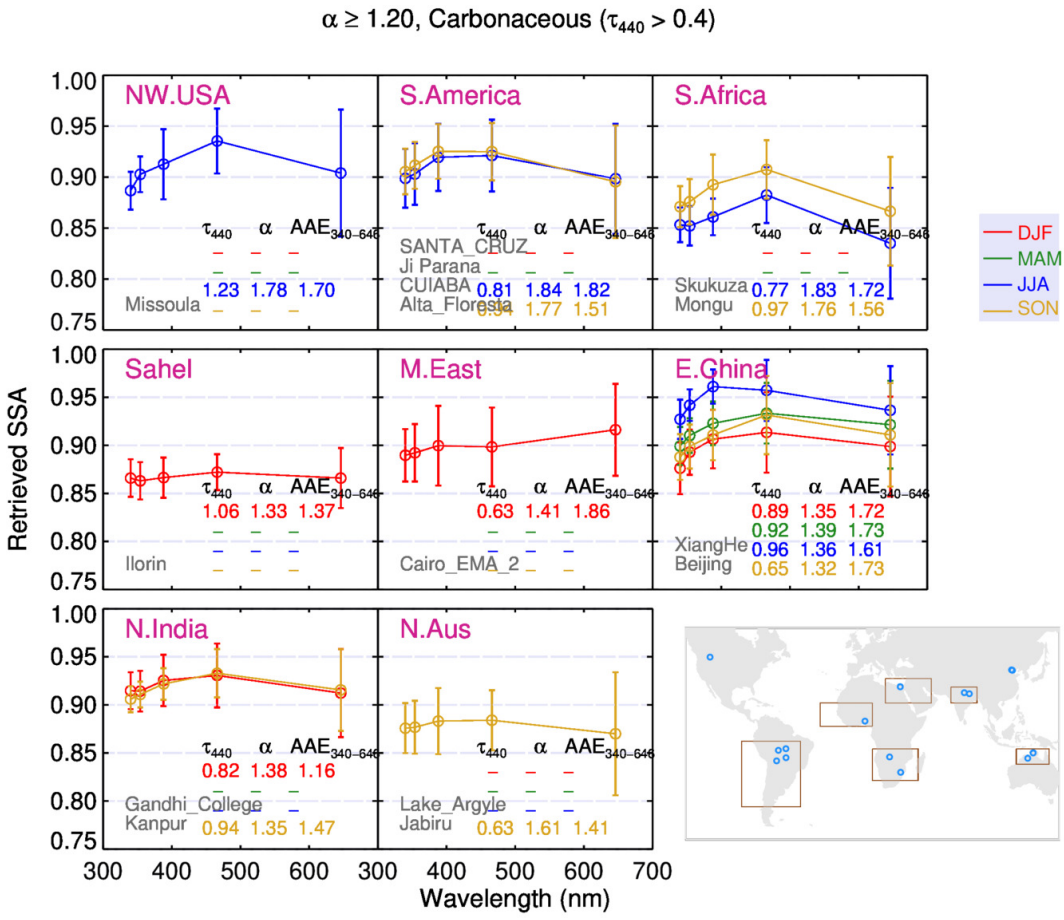

Figure 12. Seasonal average of spectral aerosol SSA derived for observations with $\tau_{440} > 0.4$ over regions dominated by fine-mode carbonaceous aerosols. The error bars represent the standard deviation of the observations.

aerosols increases from 340 to 466 nm and then decreases at longer wavelengths. Distinct seasonality in absorption for carbonaceous particles is observed with a maximum (minimum) value of 0.87 ± 0.02 (0.90 ± 0.03) at 466 nm for the JJA (SON) months. The range of regional average values of τ_{440} and $\alpha_{440-870}$ for these aerosols is about 0.76 to 1.00 and 1.76 to 1.83 ranges, respectively. The average $AAE_{340-646}$ of these carbonaceous aerosols is noted to be ~ 1.72 and 1.56 for JJA and SON months.

For the sample obtained over the Sahel region, carbonaceous aerosols are observed at Ilorin during DJF. Fine-mode aerosols observed over Ilorin are primarily emitted from the biomass burning of the grasslands and savanna in Sahelian and Sudanian zones during the dry season (November through March). Our results show these aerosols exhibit significant absorption with the average SSA $\sim 0.86 \pm 0.02$ and 0.87 ± 0.03 at 340 and 646 nm, respectively. Average τ_{440} and $\alpha_{440-870}$ are about 1 and 1.3 respectively with a mean $AAE_{340-646}$ of 1.37 for the DJF period. The high aerosol absorption noted here is consistent with the AERONET data analysis that reports high aerosol absorption with increasing fine-mode fraction (FMF) of particles (SSA $\sim$ 0.80–0.87 and 0.81–0.85 at 440 and 675 nm for observations with FMF of $0.75 - 0.54$ at 675 nm) over Ilorin during the dry season (Eck et al., 2010). The relatively low $\alpha_{440-870}$ (1.3) and nearly invariant spectral SSA through the UV-to-visible range suggests the aerosols noted over Ilorin during DJF are mixtures of black carbon and dust particles. Emissions from burning of grasslands and savanna in the Sahelian and Sudanian zones dominantly happen through flaming phase combustion producing high amounts of soot (Eck et al., 2010). In addition to the biomass burning, fossil fuel combustion, and vehicular emissions, the vast number of gas flaring stations (> 300) around the Niger Delta produce high emissions (Onyeuwaoma et al., 2015). Highly absorbing black carbon amounts observed at Ilorin are likely a result of such emissions.

For the Cairo site in the Middle East, carbonaceous aerosols are noted in our sample. Cairo in the Middle East is one of the highly polluted places among the megacities worldwide. Carbonaceous aerosols over Cairo are primarily emitted from burning of the agricultural waste in the Nile

Delta during the burning season from September through December (El-Metwally et al., 2008). Emissions from agricultural waste during the burning season add additional aerosol burden over Cairo to the prevailing high pollution levels throughout the year. The average SSA for these aerosols ranges from 0.89 ± 0.03 to 0.91 ± 0.05, exhibiting weak spectral dependence from 340 to 646 nm. Average τ_{440} and $\alpha_{440-870}$ are about 0.6 and 1.4 respectively, with $AAE_{340-646}$ about 1.9 during DJF. The spectral dependence noted for these aerosols likely indicates a mixture of black and organic carbon amounts.

Over northeastern China, carbonaceous aerosols are observed throughout the year at the Beijing and Xianghe sites from our sample. Prevailing aerosol loading over these sites constitutes emissions from biomass burning during the SON, episodic dust outbreaks during MAM, and the industrial/vehicular emissions throughout the year. The spectral behavior of carbonaceous aerosols at these sites shows an increase in SSA from 340 to 466 nm and thereafter remains near constant or slightly decreases with an UV–Vis dependence ($AAE_{340-646}$) ranging from 1.60 to 1.74. However, significant seasonality is noted with minimum (0.96 ± 0.03 at 466 nm) and maximum (0.92 ± 0.04 at 466 nm) absorption during JJA and DJF, respectively. The increase in SSA is likely a result of humidification and secondary aerosol processes during JJA. The high aerosol absorption noted during winter (DJF) is likely contributed by high amounts of local fossil fuel combustion and agricultural waste burning.

For the sample obtained over northern India, carbonaceous aerosols are observed over Kanpur and Gandhi College during SON and DJF. Emissions from crop residue burning during SON and biomass burning for residential heating in DJF prevail over the entire Indo-Gangetic Plain and likely result in such absorption. Regionally brick kilns and power plants located in the vicinity contribute to significant aerosol emissions. In addition, other industrial activities and vehicular emissions are observed throughout the seasons. The spectral behavior of these aerosols shows an increase in average SSA from 340 nm (0.91 ± 0.02) to 466 nm (0.93 ± 0.03) and a slight decrease to 646 nm (0.91 ± 0.04). The regional average $AAE_{340-646}$ for carbonaceous aerosols ranges from 1.2 to 1.5. The weak spectral dependence of SSA noted here is consistent with AERONET SSA analysis. For the aerosols observed over the Kanpur site, spectral dependence of aerosols becomes nearly invariant (SSA ~ 0.89 at 440 and 675 nm) for a high fine-mode fraction (FMF ~ 0.85) of aerosols (Eck et al., 2010).

Over northern Australia, carbonaceous aerosols are observed at the sites Jabiru and Lake_Argyle during SON. In general, northern and western parts of Australia are covered with savanna grasslands, woodlands, and forests, where biomass burning due to natural fires and land management practices is known to produce high aerosol emissions during the dry season (Scott et al., 1992; Mitchell et al., 2013). Our results indicate the average SSA for carbonaceous aerosols over northern Australia increases with wavelength from 0.87 ± 0.02 (340 nm) to 0.89 ± 0.03 (388 nm) and then decreases to 0.87 ± 0.06 (646 nm). Average τ_{440} and $\alpha_{440-870}$ for these aerosols is 0.63 and 1.61, respectively, while the UV–Vis spectral dependence ($AAE_{340-646}$) is noted to be ~ 1.41. Such behavior of fine-mode particles is likely a result of a mixture of black carbon and organic carbon amounts in the atmosphere, producing stronger (weaker) absorption in the UV (Vis) wavelengths.

6.2 Dust

For dust aerosols, minerals such as hematite and other forms of oxides play role in scattering/absorption of particles. The absorbing nature of pure dust aerosols close to the source is more sensitive to the presence of hematite than other minerals at shorter wavelengths (Sokolik and Toon, 1999). In addition to the sedimentation of coarse aggregates, the dust aerosols observed away from the source are sometimes found to have mixed (internally or externally) with anthropogenic aerosols, altering their absorbing nature. Studies show that the typical spectral behavior of dust absorption decreases with increasing wavelength primarily due to the larger size of the particles (Sokolik and Toon, 1996, 1999). However, the absorption of dust from different sources is known to vary depending on the mineral composition of the soil origin (Di Biagio et al., 2019). The seasonal average of spectral SSA for coarse-mode dust aerosols found over major aerosol environments is shown in Fig. 13.

For the dust aerosol sample obtained at the Sahara region sites Tamanrasset and Saada, the average SSA is ~ 0.94 at 466 nm. The average SSA for these dust aerosols increases with wavelength from about 0.86 ± 0.03 at 340 nm to 0.97 ± 0.02 at 646 nm. The seasonal average $AAE_{340-646}$ for dust aerosols derived at these sites ranges from 2.7 to 3.3 with no distinct seasonality in the average spectral SSA. Dust aerosols over the Middle East are observed for the sites Cairo, Solar Village, and SEDE_BOKER with an average SSA $\sim 0.95 \pm 0.02$ at 466 nm. From UV (340 nm) to visible (646 nm), the regional average SSA for dust over the Middle East sites ranges from 0.89 ± 0.03 to 0.98 ± 0.02, while the $AAE_{340-646}$ ranges from 2.7 to 3.8. No distinct seasonality in SSA is found from our sample for the dust aerosols over the Middle East. However, a slight increase in SSA at UV wavelengths is noted during winter (DJF). Examining individual sites reveals this feature corresponds to the aerosols over Solar_Village (Table S1). The increase in SSA and high $AAE_{354-388}$ noted for Solar_Village during DJF likely indicates transport of aerosols from neighboring regions.

Over the Sahel, dust aerosols are observed for several sites that include Agoufou, Banizoumbou, Dakar, IER_Cinzana, Ilorin, Ouagadougou, and Zinder_Airport. Located in the middle of the Sahelian region through the west Africa, these sites are influenced by both dust and biomass burning emissions (Basart et al., 2009). It should be noted that for the

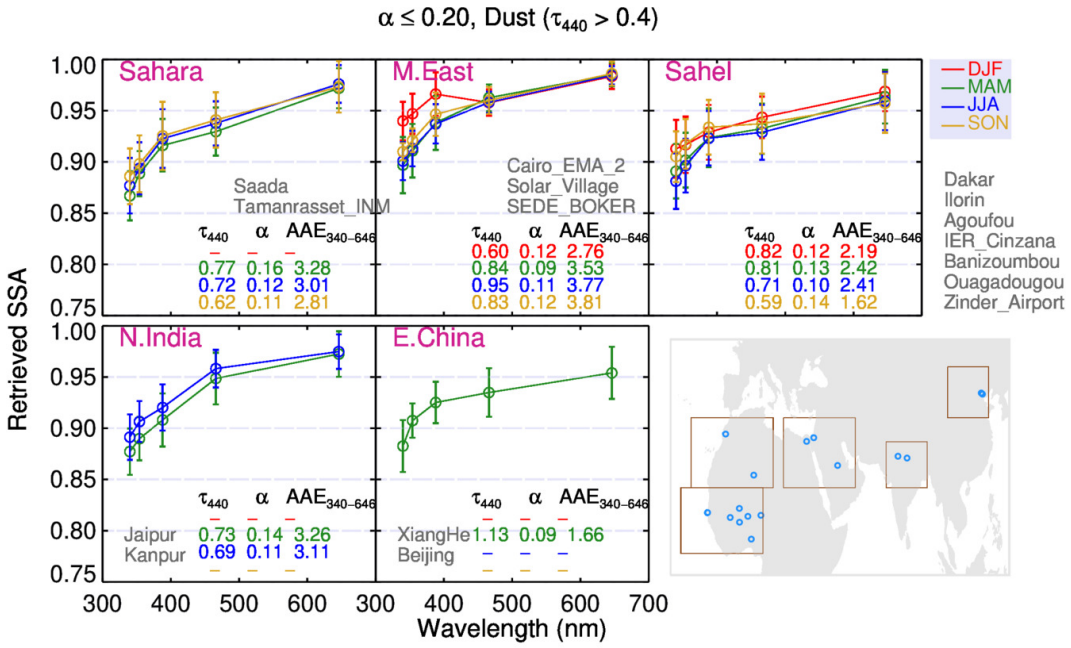

Figure 13. Seasonal average of spectral aerosol SSA derived for observations with $\tau_{440} > 0.4$ over regions dominated by coarse-mode dust aerosols. The error bars represent the standard deviation of the observations.

identifying dust in this work, we use $\alpha_{440-870} \leq 0.2$ derived from AERONET. The regional average spectral SSA for dust aerosols derived here resembles a typical dust absorption curve (increase in SSA with wavelength, ~ 0.87–0.91 ± 0.03 at 340 nm to 0.95–0.97 ± 0.02 at 646 nm) with absorption ranging $\sim 0.93 - 0.94 \pm 0.02$ at 466 nm. No distinct seasonality in absorption of dust aerosols is noted over the Sahel. Average $AAE_{340-646}$ for dust over the Sahel ranges from 2.0 to 2.3 for all seasons, except during SON, where $AAE_{340-646}$ is noted to be relatively lower at 1.57.

Over northern India, dust aerosols are observed during spring (MAM) and summer (JJA) months for the sites at Jaipur and Kanpur, where the former site is in proximity to the Thar Desert and the later site is influenced by the dust transport. The average SSA shows a steep increase from 340 nm (0.88 ± 0.02) to 466 nm (0.95 ± 0.03) and a relatively smaller increase from 466 to 646 nm (0.97 ± 0.02). The dust aerosols noted here have an average τ_{440} of 0.73 to 0.77 and exhibit $AAE_{340-646}$ between 2.9 and 3.4. Compared to AERONET the absorption for dust aerosols derived here agrees well. Eck et al. (2010) reports the coarse-mode particles noted over Kanpur during pre-monsoon (MAM) months exhibit climatological average SSA ~ 0.89 and 0.95 at 440 and 675 nm, respectively.

For the samples obtained over northeastern China, dust aerosols are observed over Beijing and Xianghe during spring (MAM). The spectral curve of regional average SSA shows an increase from 0.87 ± 0.03 at 340 nm to 0.95 ± 0.03 at 646 nm. The average $AAE_{340-646}$ obtained for the dust aerosols at these sites is 1.56. Among the regional dust observations presented here (Fig. 12), northeastern China exhibits high absorption in visible wavelengths ($\omega_o \sim 0.93 \pm 0.03$ and 0.95 ± 0.03 at 466 and 646 nm) and low $AAE_{340-646}$. It is likely that these coarse particles are influenced by black carbon components over such highly polluted environments and exhibit anomalously low AAE compared to dust particles noted for other regions. However, due to large particle size ($\alpha_{440-870} \sim 0.09$) the spectral SSA noted still shows increasing SSA with wavelength. Chaudhry et al. (2007) reported in situ measurements of coarse-mode particles over Xianghe during March 2005 that exhibit high absorption in visible wavelengths ($\omega_o \sim 0.70$–0.94 at 450, 550, and 700 nm). Li et al. (2007) explained the variation in SSA for coarse particles during March 2005 over Xianghe is a result of synoptic fluctuation – passage of cold fronts that uplifted ground-level pollution to higher altitudes influencing the aerosol absorption. Similar low $AAE_{340-646}$ values for coarse mode ($\alpha_{440-870} < 0.2$, dust) are noted for the few sites over the Sahelian region during DJF (burning season). It is likely that these coarse particles are influenced by black carbon amounts emitted from biomass burning.

6.3 Urban–industrial aerosols

Urban aerosols dominantly constitute sulfates and other forms of nitrate particles. Additionally, industrial emissions and fossil fuel combustion produce various forms of carbon (organic and black carbon) that contribute to the overall optical properties of urban aerosols. Further, the aerosol size growth due to the increase in relative humidity in the atmo-

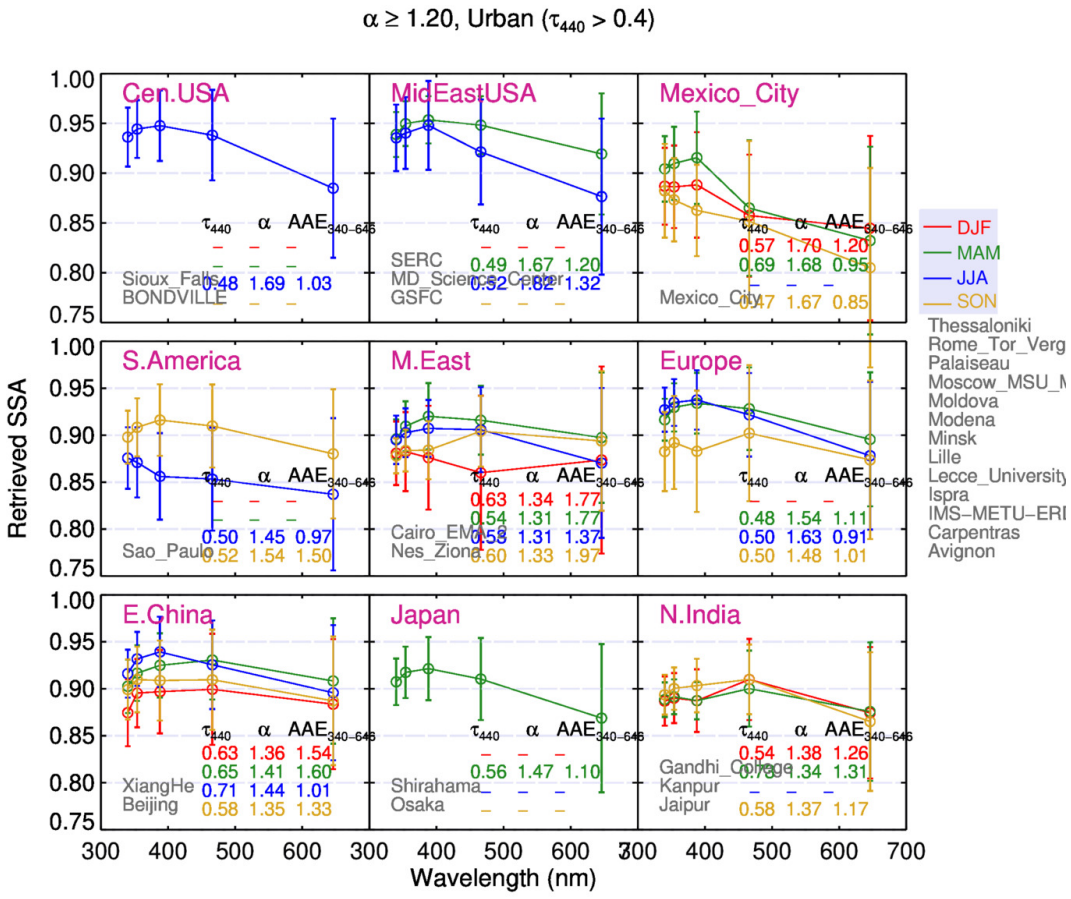

Figure 14. Seasonal average of spectral aerosol SSA derived for observations with $\tau_{440} > 0.4$ over regions dominated by fine-mode urban or mixture of aerosols. The error bars represent the standard deviation of the observations.

sphere and coagulation processes is known to alter the absorbing nature of aerosols. The typical spectral SSA of urban aerosols decreases with an increase in wavelength from the UV–Vis spectrum (Bergstrom, 1972). The seasonal average of spectral SSA for carbonaceous aerosols found over major aerosol environments is shown in Fig. 14.

Aerosols observed over the central United States (US) at the sites Sioux Falls and Bondville are primarily produced from industrial activities and vehicle emissions. The average aerosol SSA for these urban aerosols shows an increase (0.93–0.95 ± 0.03) in the wavelength range 340-388 nm followed by a decrease (0.89 ± 0.06 at 646 nm) towards the visible wavelengths. Average τ_{440} and $\alpha_{440-870}$ are about 0.48 and 1.7, respectively, while the average $AAE_{340-646}$ is noted as 1.1. Urban aerosols over the mid-eastern US are noted for the sites at GSFC, MD_Science_Center, and the Smithsonian Environmental Research Center (SERC). The average aerosol SSA noted for these sites increases from (0.93±0.02) 340 nm to (0.95 ± 0.03) 388 nm and then decreases attaining a maximum absorption (∼ 0.87 ± 0.06) at 646 nm. The regional average SSA for the MAM and JJA months at 466 nm is 0.94 ± 0.03 and 0.92 ± 0.03, respectively. Seasonally, the average SSA noted for JJA follows a typical urban absorption curve, while the spectral SSA shows a decrease in aerosol absorption in the visible wavelengths for MAM. Since there are no significant changes in aerosol sources during MAM and JJA over the mid-eastern US, the seasonal variation in SSA noted for visible wavelengths likely stems from a weak absorption signal which is insufficient for a robust retrieval or partially due to poor sample size. Recall that for weakly absorbing aerosols the error in SSA retrievals at visible wavelengths is high due to identified factors from our analysis such as cloud contamination, surface reflectance, and particle size.

For the site in Mexico City, Mexico, urban aerosols are noted in our sample. In general, Mexico City is a densely populated urban location that is well known for its high pollution levels among the other megacities worldwide. In addition to the high concentration of aerosols from fossil fuel combustion throughout the year, Mexico City also experiences biomass-burning aerosols during the relatively dry months of March–May from local sources. The seasonal average aerosol SSA over Mexico City shows a decrease in absorption in the UV (0.90 ± 0.03 and 0.91 ± 0.05 at 340

and 388 nm) and increases towards the visible wavelengths during MAM. However, the spectral SSA noted for DJF (0.88 ± 0.04 and 0.87 ± 0.05 at 340 and 388 nm) and SON (0.88 ± 0.04 and 0.85 ± 0.05 at 340 and 388 nm) deviates from known pattern and exhibits high absorption in the UV spectral range with a nearly constant or slight increase in the visible spectral range. The average SSA values at 466 nm for DJF, MAM, and SON months are 0.85 ± 0.06, 0.86 ± 0.06, and 0.84 ± 0.06, respectively, with average $\alpha_{440-870}$ about 1.7 throughout the seasons. Although the seasonal average $AAE_{340-646}$ of aerosols over Mexico City ranges from 0.94–1.27, the $AAE_{354-388}$ is higher for (5.13) MAM compared to (2.2) DJF and (0.6) SON months. It is likely that our aerosol samples obtained during MAM are influenced by biomass burning emissions from local neighbor sources exhibiting high $AAE_{354-388}$ values, suggesting the absorption is driven by organic components (Barnard et al., 2008), whereas for the samples noted during SON and DJF the aerosol absorption is primarily driven by the black carbon components emitted from the heavy industrial and vehicular fleet over the region.

Our subset of samples noted urban aerosols at the site São Paulo, South America. São Paulo is the largest megacity in South America with a population exceeding 21 million inhabitants. Heavy industrial and vehicular emissions are the dominant source of aerosols observed over São Paulo. In addition, aerosols from the northern parts of the Amazon Basin advecting south or southeast over São Paulo are not uncommon during the peak burning season (August–September). Average τ_{440} and $\alpha_{440-870}$ noted for these aerosols are $\sim$ 0.57 and 1.5, respectively, during JJA and SON months. The spectral SSA noted here resembles a typical urban absorption curve during SON. However, during JJA spectral SSA shows a steep decrease from 340 to 388 nm (0.87 ± 0.03 to 0.85 ± 0.03) and remains nearly invariant towards the visible spectral range from 466 to 646 nm (0.85 ± 0.05 to 0.84 ± 0.07). The average SSA noted at 466 nm is 0.88 ± 0.06 (0.92 ± 0.06) for JJA (SON) months. Our results indicate that the urban aerosols at São Paulo are more absorbing during JJA than in SON, and it is likely that mixing of carbonaceous and urban aerosol samples caused this feature.

For the urban aerosols observed over Cairo and Ness Ziona in the Middle East, the average SSA is noted to be 0.89 ± 0.03 at both 340 and 646 nm. While urban aerosols and pollution prevail over Ness Ziona, emissions from crop residue burning (rice straws) over the Nile Delta region during winter (DJF) and heavy pollution dictate the aerosol absorption noted over Cairo. Average τ_{440} and $\alpha_{440-870}$ noted for these aerosols are $\sim$ 0.60 and 1.3, respectively, throughout the seasons, with mean $AAE_{340-646}$ ranging between 1.5–2.0. Unlike a typical urban aerosol absorption curve, the spectral SSA values noted for these aerosols do not exhibit a steep decrease from 388 to 646 nm, indicating a mixture of dust and carbonaceous particles.

Over Europe, dominantly urban aerosols are observed at the sites Avignon, Carpentras, Ispra, IMS-METU-ERI, Lille, Lecce_University, Minsk, Modena, Moldova, Moscow_MSU, Palaiseau, Rome, and Thessaloniki. Primarily industrial activities and vehicular emissions are the dominant sources of aerosols over Europe. In addition, fuel combustion for residential heating during winter and episodic dust transported during spring–summer over the Iberian Peninsula and Mediterranean Basin are known to influence the aerosol loading (Basart et al., 2009; Mallet et al., 2013). The regional average SSA increases from 340 nm (0.91 ± 0.02) to 388 nm (0.93 ± 0.03) and then decreases, reaching a minimum value (0.87 ± 0.07) at 646 nm for most seasons. The observed aerosol absorption is similar for spring (MAM) and summer (JJA). However, there is an increase in absorption at wavelengths other than 646 nm for fall (SON) that reaches a maximum absorption 0.86 ± 0.03 and 0.90 ± 0.04 at 340 and 466 nm, respectively. These highly absorbing aerosols in our sample are noted over polluted urban sites at Ispra, Modena, and Rome from northern to central Italy and are likely a result of mixtures of pollution and carbon particles from wood burning for domestic heating during fall and the winter months. Our results are consistent with that showing a decrease in aerosol SSA over Ispra, northern Italy, during fall and winter (Putaud et al., 2014). Average τ_{440} and $\alpha_{440-870}$ noted for these aerosols are $\sim$ 0.50 and 1.5, respectively, throughout the seasons, with mean $AAE_{340-646}$ ranging between 1.0–1.3.

Over northeastern China, urban aerosols are noted for the sites Beijing and Xianghe. Significant seasonality in aerosol SSA is noted with minimum (0.93 ± 0.04 at 466 nm) and maximum (0.88 ± 0.05 at 466 nm) absorption during JJA and DJF, respectively. Seasonal variability in aerosol absorption noted here is likely caused by the humidification and secondary aerosol processes. In addition to the high industrial and vehicular emissions throughout the year, fuel combustion for residential heating purposes and agricultural waste burning during DJF adds additional aerosol burden over northeastern China. High aerosol absorption noted during DJF is likely a result of such emissions. Average τ_{440} and $\alpha_{440-870}$ noted for these aerosols are $\sim$ 0.65 and 1.4, respectively, throughout the seasons, with mean $AAE_{340-646}$ ranging between 1.2–1.7. For the urban aerosols noted at the sites Shirahama and Osaka in Japan during MAM, the spectral aerosol SSA noted follows a typical urban absorption curve with a slight increase in SSA from (0.90 ± 0.02) 340 nm to (0.92 ± 0.02) 388 nm and then a steep decrease towards (0.87 ± 0.07) 646 nm. Average τ_{440} and $\alpha_{440-870}$ noted for these aerosols are $\sim$ 0.5 and 1.5, respectively, with mean $AAE_{340-646}$ about 1.2.

Over northern India, urban aerosols are noted for the sites at Jaipur, Kanpur, and Gandhi College. Major sources of aerosols over the region include industrial and vehicular emissions, combustion of biomass and fossil fuels, and seasonally occurring agricultural burning. The average aerosol

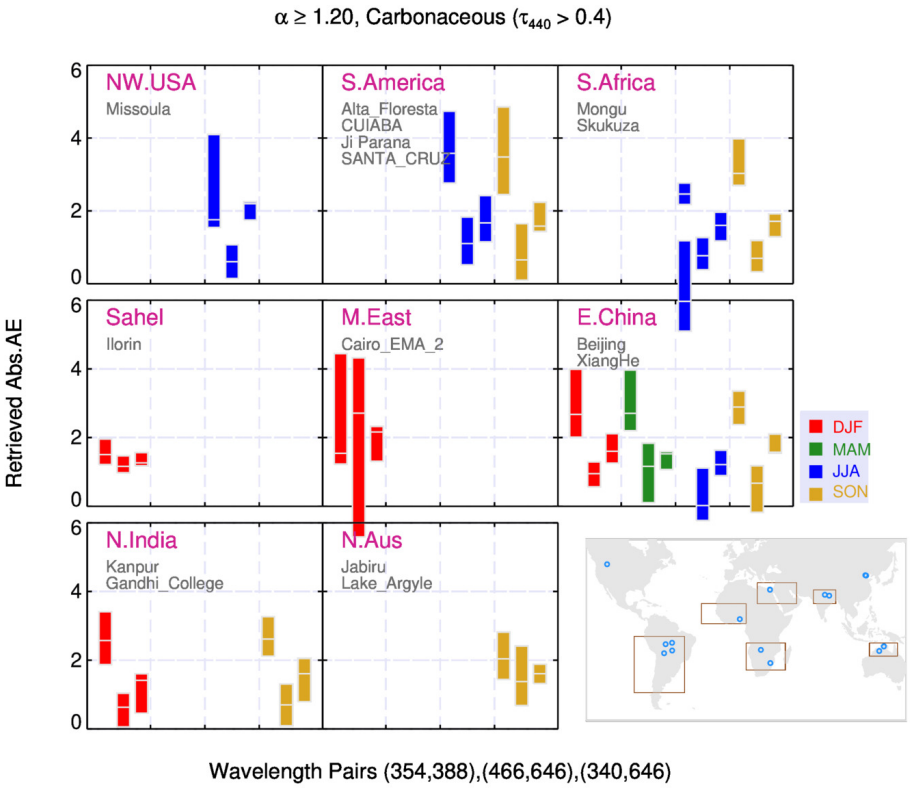

Figure 15. Absorption Ångström exponent derived at three wavelength pairs for observations with $\tau_{440} > 0.4$ for the fine-mode carbonaceous aerosols. The boxplot represents the lower and upper quartile of observations with the mean as the white line.

SSA increases from (0.88 ± 0.02) 340 nm to (0.90 ± 0.04) 466 nm and decreases towards 646 nm (0.87 ± 0.07) 646 nm. These aerosols are noted to exhibit relatively high absorption $\omega_o \sim 0.89 \pm 0.04$ at 466 nm. Average τ_{440} and $\alpha_{440-870}$ noted for these aerosols are ~ 0.60 and 1.4, respectively, throughout the seasons, with mean $AAE_{340-646}$ about 1.3. Throughout the seasons, the influence of pollution aerosols is clearly evident in the observed aerosol absorption.

7 Discussion

Through extensive studies in the literature, it is known that optical properties of biomass burning aerosols depend on fuel/vegetation type, combustion processes, and available moisture content (e.g., Ward, 1992; Reid and Hobbs, 1998; Reid et al., 1998; Eck et al., 2001). Such studies reported varying properties of aerosols emitted from the two phases of vegetation burning: flaming and smoldering. While the flaming phase rapidly oxidizes the available volatile hydrocarbons in the biomass, the smoldering phase mostly requires a surface where slow diffuse oxygen converts the biomass through exothermic reaction. In general, burning of grasslands happens dominantly through flaming phase combustion that emits high amounts of black carbon, while smoldering phase combustion is prevalent in the burning of woodlands/deciduous forest that emits less black carbon and more organic carbon. The observed aerosol absorption at the biomass burning sites (Fig. 12) clearly makes this distinction. Over South America, in addition to the emissions from burning rainforest (nearby Alta Floresta and Ji-Paraná), Cerrado (wooded grasslands) type vegetation dominates at the CUIABA-MIRANDA site (Schafer et al., 2008). Biomass burning of tropical forests occurs through smoldering combustion exhibiting aerosol ω_o $(0.93 \pm 0.03$ at 466 nm). Compared to South America, the aerosols over southern Africa have distinct seasonality and high absorption ($\omega_o \sim 0.88 \pm 0.02$ at 466 nm). Eck et al. (2013) demonstrated that this seasonality in aerosol absorption is likely a result of a shift in fuel type and combustion process. At the beginning of the dry season (starting June), the savanna grasses in the central region are prone to undergo a rapid burning through flaming process, while in the late dry season (ends November) the wooded lands located in southeastern parts begin to burn dominantly through smoldering phase combustion. For the savanna with open grasslands in northern Australia, biomass burning happens dominantly through flaming phase combustion producing high amounts of soot, as also noted in our retrievals. Figure 15 shows the range of AAE obtained for carbonaceous aerosols at three wavelength pairs. Overall, the average slope of absorption in visible ($AAE_{466-646}$) and UV–

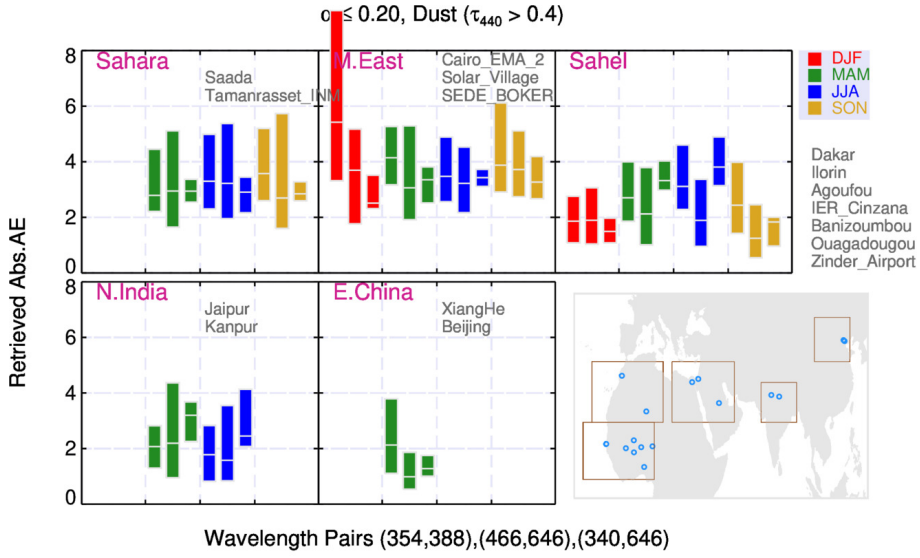

Figure 16. Absorption Ångström exponent derived at three wavelength pairs for observations with $\tau_{440} > 0.4$ for the coarse-mode dust aerosols. Boxplot represents the lower and upper quartile of observations with the mean as the white line.

Vis ($AAE_{340-646}$) for carbonaceous aerosols is found to be within 2. This is consistent with the studies that report AAE of biomass burning aerosols from several field campaigns in the range 1 to 3 (Kirchstetter et al., 2004; Schnaiter et al., 2005; Bergstrom et al., 2007; Clarke et al., 2007). However, the average $AAE_{354-388}$ obtained is high – up to 4 for most regions. This is likely a result of higher organic matter in the regional biomass types and highlights the importance of the UV spectral region in delineating such a group of aerosols. Despite high errors in the estimated uncertainties of AAE computation over the narrow spectral range 354 to 388 nm, our results are consistent with studies showing that spectral dependence of aerosol absorption in the UV–visible range can be high – up to 6 for aerosols with organic compounds (Kirchstetter et al., 2004; Bergstrom et al., 2007, and references therein). Among the biomass burning regions, for the emissions where the contribution of flaming phase combustion is high, the mean $AAE_{354-388}$ noted is relatively low: 2.1 in northern Australia and 1.6 in the Sahel. Further, it is noted that carbonaceous aerosols observed over northern India, northeastern China, the Sahel, and the Middle East have an average $\alpha_{440-870} \sim 1.4$ (i.e, at the lower end of the fine-mode range), while in South America, South Africa, and Australia they have an average ~ 1.8. This indicates that other than aerosol composition, processes such as aerosol mixing (for example mixing of dust in the Sahel), aging, and humidification (for example aerosols observed during summer over northeastern China) play a role in the observed variability of aerosol absorption.

Figure 16 shows the range of AAE obtained for dust aerosols at three wavelength pairs. Regional average of the UV–Vis spectral dependence ($AAE_{340-646}$) is found to be close to or greater than 3 for all regions, except for the Sahel and northeastern China, where average value ranges from 1.5 to 2.5. Although no distinct seasonal variation in spectral absorption of dust is noted, the variability in spectral dependence over the regions is quite evident. The regional average of SSA for dust aerosols from 340 nm to 646 nm is 0.87 ± 0.02 to 0.98 ± 0.02, 0.89 ± 0.03 to 0.96 ± 0.02, 0.89 ± 0.02 to 0.98 ± 0.01, 0.87 ± 0.02 to 0.97 ± 0.02, and 0.87 ± 0.03 to 0.95 ± 0.03 over the Sahara, the Sahel, the Middle East, northern India, and northeastern China, respectively. While the average SSA ranges from 0.87 to 0.89±0.03 at 340 nm, differences in retrieved SSA are evident with increasing wavelength. The regional average spectral SSA noted at 466 nm is 0.94 ± 0.02, 0.93 ± 0.02, 0.96 ± 0.02, 0.95 ± 0.02, and 0.93 ± 0.02 for the Sahara, the Sahel, the Middle East, northern India, and northeastern China, respectively. A recent study uses soil samples collected from different arid regions worldwide to characterize the mineral composition of dust and estimate the spectral SSA using the measured scattering absorption coefficients through an Aethalometer operating at seven discrete wavelengths from 370–950 nm (Di Biagio et al., 2019). Their study reports high absorption ($\sim$0.70–0.75 at 370 nm) for dust samples obtained over Niger, Mali, southern Namibia, and Australia due to the presence of higher amounts of iron oxides, whereas for the samples collected over Bodélé, northern Namibia, and Arizona the estimated absorption ($\sim$0.91–0.96 at 370 nm) and amounts of iron oxides are relatively low. In comparison, our retrievals indicate the dust aerosols noted at the Sahel and northeastern China are highly absorbing, while those noted over the Middle East and northern India are less absorbing, and dust over the Sahara shows intermediate absorption. These results can be explained by combination of varying mineral composition (iron oxide amounts) and mixing of

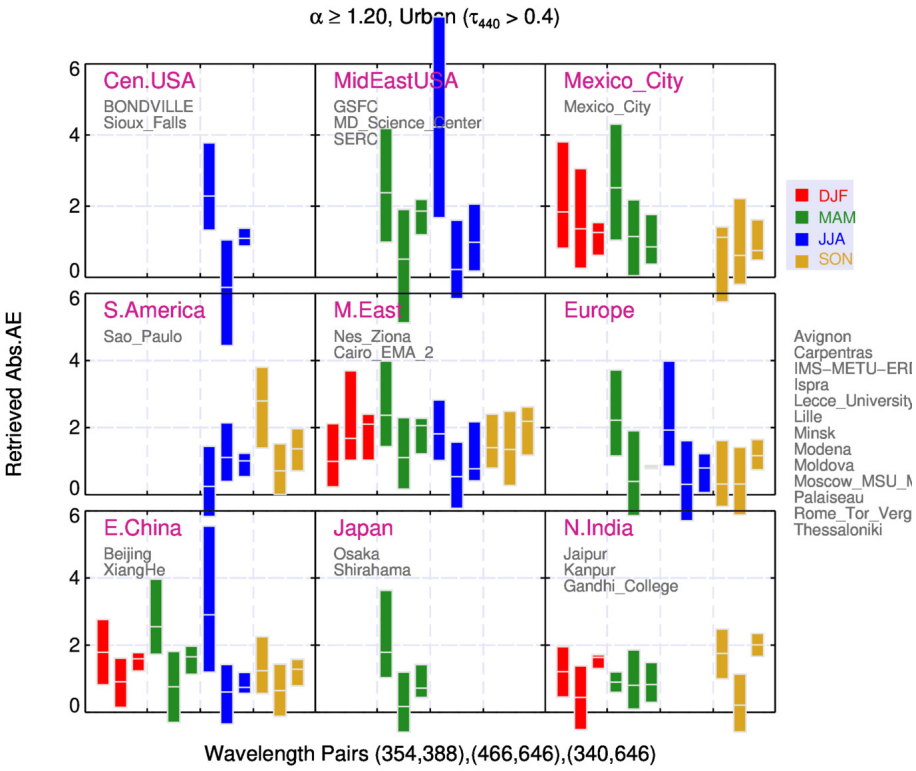

Figure 17. Absorption Ångström exponent derived at three wavelength pairs for observations with $\tau_{440} > 0.4$ for the fine-mode urban or mixture of aerosols. Boxplot represents the lower and upper quartile of observations with the mean as the white line.

dust with other sources along the transport pathway. However, the magnitude of SSA and AAE reported by Di Biagio et al. (2019) is lower than that retrieved here for all regions. The reason for the differences noted in SSA is unknown and needs further investigation. In contrast, our retrieved SSA for coarse-mode particles agrees well with AERONET SSA (59 % and 87 % observations within ±0.05 envelopes at 466 and 646 nm respectively). Overall the regional average of AAE for dust aerosols observed here is consistent with in situ measurements (Bergstrom et al., 2004, 2007; Müller et al., 2009; Petzold et al., 2009) that report values ranging 2.0 to 3.5. Observations at individual sites (Table S1) show that the spectral dependence of the observed dust for few sites is relatively high compared to those reported by in situ measurements. Considering our retrieval method where aerosol absorption is derived independently for each wavelength and has computed the dependence, our results agree reasonably well with the in situ measurements reported in the literature.

Figure 17 shows the regional average AAE obtained for urban aerosols at three wavelength pairs. Urban aerosols in highly polluted environments such as over Mexico City have near-unity spectral dependence, whereas the passage of biomass burning emissions over such environment shows an unusual decrease in absorption at the UV region due to high $AAE_{354-388}$. This is consistent with studies that report relatively high AAE in the UV region and near unity in the visible region for the aerosol mixture consisting of organic matter and black carbon amounts (Barnard et al., 2008; Martins et al., 2009; Bergstrom et al., 2010; Jethva and Torres, 2011). The urban aerosols found in our sample over northern Indian and northeastern China are highly absorbing, exhibiting $AAE_{340-646} \sim 1.5$ than the carbonaceous aerosols with $AAE_{340-646} \sim 2$. These results suggest the combination of the magnitude of aerosol absorption and its spectral dependence in the UV, visible, and UV–visible spectrum could be used to partition the mixture of aerosol types found in such environments. Overall, the regional average UV–visible AAE for the urban aerosols is found to be near 2.

8 Summary

Ground-based measurements of direct and diffuse solar radiation under cloud-free conditions over worldwide sites provide valuable insights into regional aerosol characteristics. Long-term measurements obtained from networks such as AERONET are widely used to develop regional aerosol climatology and investigate seasonal/annual variability, in addition to providing validation data sets for the satellite-based AOD retrievals. Satellite measurements of TOA radiances are able to provide global distribution of columnar aerosol amounts. However, deriving aerosol optical properties from

satellite measurements requires constraints on particle sizes and optical properties. Reliable aerosol measurements from ground networks and airborne/field campaigns are traditionally used to validate and improve the constraints in satellite aerosol retrievals.

In this work, we use the AERONET-measured extinction τ as a constraint in a robust inversion technique that uses satellite-measured TOA radiances from OMI and MODIS to derive spectral aerosol absorption in the UV–Vis part of the spectrum. Other than cloud contamination of the TOA radiances, major sources of error in our retrieved SSA come from surface reflectance and aerosol layer height. We use TOA radiance observations with minimal or no cloud contamination reported by both OMI and MODIS products. Sensitivity tests show that our retrieved aerosol SSA has a reliable accuracy up to ± 0.04 from UV–visible wavelengths for absorbing aerosols (carbonaceous and dust) with $\tau_{440} > 0.4$. However, for less-absorbing aerosols the error in SSA retrieval reaches up to ± 0.07. Using a subset of results where SSA is retrieved independently for 340, 354, 388, 466, and 646 nm wavelengths for the same day with observations $\tau_{440} > 0.4$, we examine the seasonal variability in aerosol SSA and derive spectral dependence (AAE) at three wavelength pairs in the UV–Vis spectrum.

Key observations noted from the spectral aerosol absorption data set derived here are shown below.

- Carbonaceous aerosols
  a. Among sites dominated by biomass burning aerosols, Mongu in southern Africa has high absorption $\omega_o \sim 0.85 \pm 0.02$ and 0.84 ± 0.05 at 340 and 646 nm, respectively.
  b. Strong seasonality in absorption of carbonaceous aerosols is evident in southern Africa, indicating the role of biomass types and combustion processes. The average ω_o values noted at 340 and 646 nm during JJA (SON) are $\sim 0.85 \pm 0.02$ (0.88 ± 0.02) and 0.84 ± 0.05 (0.87 ± 0.05), respectively.
  c. Carbonaceous aerosols found over northern Australia are as strongly absorbing ($\omega_o \sim 0.87 \pm 0.03$ and 0.86 ± 0.06 at 340 and 646 nm) as smoke over southern Africa but have nearly invariant ω_o from UV–Vis spectra.
  d. Carbonaceous aerosols found over Alta_Floresta in the Amazon Basin have similar absorption ($\omega_o \sim 0.89 \pm 0.02$ and 0.91 ± 0.06 at 340 and 646 nm) and $AAE_{340-646}$ (1.8) to those found over Missoula in the northwestern US.
  e. Highly absorbing carbonaceous aerosols with weak spectral dependence are found in Cairo ($\omega_o \sim 0.89 \pm 0.02$ and 0.91 ± 0.06 at 340 nm and 646 nm) and Ilorin ($\omega_o \sim 0.86 \pm 0.02$ and 0.87 ± 0.03 at 340 and 646 nm) during winter (DJF) in the Middle East and Sahel respectively.
  f. Carbonaceous aerosols found over northern India ($\omega_o \sim 0.91 \pm 0.02$ and 0.92 ± 0.04 at 340 and 646 nm), northeastern China ($\omega_o \sim 0.87$–0.90 ± 0.03 and 0.90–0.94 ± 0.05 at 340 and 646 nm), the Sahel ($\omega_o \sim 0.86 \pm 0.02$ and 0.87 ± 0.03 at 340 and 646 nm), and the Middle East ($\omega_o \sim 0.89 \pm 0.03$ and 0.92 ± 0.05 at 340 nm and 646 nm) have low average $\alpha_{440-870}$ (< 1.4) compared to over other prominent biomass burning regions, suggesting a mixture of fine and coarse modes.
  g. Distinct seasonality in spectral absorption of carbonaceous aerosols is noted for northeastern China. The maximum (minimum) absorption is noted during DJF (JJA), exhibiting $\omega_o \sim 0.87 \pm 0.02$ and 0.90 ± 0.05 at 340 and 646 nm ($\omega_o \sim 0.91 \pm 0.02$ and 0.94 ± 0.04 at 340 and 646 nm), respectively.
- Dust aerosols
  a. For desert dust aerosols, the SSA is known to increase with wavelength from the UV-to-visible spectrum. No distinct seasonality in SSA is noted. The regional average of SSA for dust aerosols from 340 to 646 nm is 0.87 ± 0.02 to 0.98 ± 0.02, 0.89 ± 0.03 to 0.96 ± 0.02, 0.89 ± 0.02 to 0.98 ± 0.01, 0.87 ± 0.02 to 0.97 ± 0.02, and 0.87 ± 0.03 to 0.95 ± 0.03 over the Sahara, the Sahel, the Middle East, northern India, and northeastern China, respectively.
  b. Among the dust-dominated regions considered here, our retrievals indicate relatively high absorption ($\omega_o \sim 0.93 \pm 0.03$ at 466 nm) for aerosols noted at the Sahel and northeastern China, while those noted over the Middle East and northern India ($\omega_o \sim 0.97 \pm 0.03$ at 466 nm) are less absorbing and dust over the Sahara ($\omega_o \sim 0.95 \pm 0.02$ at 466 nm) shows intermediate absorption. These results can be explained by combination of varying mineral composition (iron oxide amounts) and mixing of dust with other sources along the transport pathway.
- Urban aerosols
  a. Urban aerosols ($\omega_o \sim 0.87 \pm 0.04$ and 0.84 ± 0.08 at 340 and 646 nm) are highly absorbing and exhibit distinct seasonality (higher absorption during JJA than SON) at São Paulo, South America. The urban aerosols noted here are likely mixtures of carbonaceous particles transported over the region and prevailing pollution from local sources.
  b. Polluted aerosols observed over Mexico City show high absorption in UV extending to the visible spectrum during DJF ($\omega_o \sim 0.88 \pm 0.04$ and 0.84 ± 0.09 at 340 and 646 nm) and SON ($\omega_o \sim 0.88 \pm 0.04$ and 0.80 ± 0.08 at 340 and 646 nm) months.

c. Polluted aerosols noted over the Cairo and Ness Ziona in the Middle East are highly absorbing and exhibit weak spectral dependence ($\omega_o \sim 0.87–0.89 \pm 0.03$ and $0.87–0.90 \pm 0.07$ at 340 and 646 nm).

d. Polluted aerosols noted over the Jaipur, Kanpur, and Gandhi College in northern India are highly absorbing and exhibit weak spectral dependence ($\omega_o \sim 0.88 \pm 0.03$ and 0.87 ± 0.07 at 340 and 646 nm).

As mentioned, the results presented here are limited to our subset of retrievals, where SSA is retrieved for all five wavelengths from a UV–visible range with $\tau_{440} > 0.4$. Since one of our objectives is to derive UV–visible spectral dependence (AAE) of aerosols, and given the inherent sampling bias of the OMI, MODIS, and AERONET collocations, the analysis method employed here is well justified. In other words, we made use of the best available data synergy and derived a unique aerosol absorption data set with no prior assumptions on wavelength dependence, which otherwise is assumed in the standard satellite-based aerosol retrieval algorithm. It should be noted that our results may be biased toward dense pollution/industrial, smoke, and dust events. In addition, the regional aerosol absorption derived here may not be representative of the entire region due to limited sampling and fewer sites used. However, these absorption models offer essential guidance for selecting spectral absorption in satellite aerosol retrievals using UV (OMI), Vis (MODIS), and even spanning the UV–Vis spectrum, as planned under the upcoming Plankton, Aerosol, Cloud, ocean Ecosystem (PACE) mission. From our analysis of worldwide inland sites (a) it is suggested that satellite aerosol retrieval techniques could employ regional dynamic absorption models to avoid potential bias in τ retrievals noted in earlier studies and (b) the spectral dependence of aerosol absorption noted here for the UV (354–388 nm), visible (466–646 nm), and UV–visible (340–646 nm) range for all aerosol types other than black carbon varies considerably. Overall, the UV absorption data set well complements and provides more information on the regional aerosol absorption than with the visible data set alone.

Given the lack of aerosol absorption information at near-UV wavelengths in the currently existing AERONET inversion products and limited availability of in situ measurements, the UV–Vis aerosol absorption data set developed here, perhaps for the first time, offers a valuable source of information useful for a variety of aerosol and trace gas studies. As mentioned earlier the newer models of AERONET sun photometers include sky radiance measurements at 380 nm, and the derived SSA at this near-UV wavelength is expected in the future upgrade of the AERONET inversion product. The derived spectral dependency can be used with either a subset of the results or all SSA retrievals to construct and investigate long-term trends in UV–visible aerosol absorption. Further, the spectral aerosol SSA derived here could be used to parameterize absorption in models and better understand the radiative effects of aerosols. Our ongoing investigation utilizing the complete data set developed here will explore some of these applications in the future.

Data availability. The spectral aerosol absorption data set developed here will be made available upon request to the authors.

Supplement. The supplement related to this article is available online at: https://doi.org/10.5194/amt-15-845-2022-supplement.

Author contributions. OT and HJ conceptualized the research. VK developed the data set, performed formal analysis, and wrote the manuscript with input from OT and HJ. All authors reviewed results, helped with the data interpretation, and edited the manuscript to make a final version.

Competing interests. The contact author has declared that neither they nor their co-authors have any competing interests.

Disclaimer. Publisher's note: Copernicus Publications remains neutral with regard to jurisdictional claims in published maps and institutional affiliations.

Acknowledgements. The authors are grateful to Brent Holben and the entire AERONET team for their efforts in maintaining AERONET sites worldwide and providing quality-assured data to the community. The authors thank all principal investigators (PIs) and co-PIs of the individual AERONET sites that were used in this work. The authors thank the three anonymous reviewers for their constructive feedback that helped to make significant improvements to the article.

Financial support. This research has been supported by NASA ROSES (ACMAP) 2016 (grant no. NNH16ZDA001N).

Review statement. This paper was edited by Daniel Perez-Ramirez and reviewed by three anonymous referees.

References

Andreae, M. O. and Merlet, P.: Emission of trace gases and aerosols from biomass burning, Global Biogeochem. Cy., 15, 955–966, https://doi.org/10.1029/2000GB001382, 2001.

Ångström, A.: On the atmospheric transmission of sun radiation and on dust in the air, Geogr. Ann., 11, 156–166, https://doi.org/10.2307/519399, 1929.

Bais, A. F., Kazantzidis, A., Kazadzis, S., Balis, D. S., Zerefos, C. S., and Meleti, C.: Deriving an effective aerosol single scattering albedo from spectral surface UV irradiance measurements, Atmos. Environ., 39, 1093–1102, https://doi.org/10.1016/j.atmosenv.2004.09.080, 2005.

Barnard, J. C., Volkamer, R., and Kassianov, E. I.: Estimation of the mass absorption cross section of the organic carbon component of aerosols in the Mexico City Metropolitan Area, Atmos. Chem. Phys., 8, 6665–6679, https://doi.org/10.5194/acp-8-6665-2008, 2008.

Basart, S., Pérez, C., Cuevas, E., Baldasano, J. M., and Gobbi, G. P.: Aerosol characterization in Northern Africa, Northeastern Atlantic, Mediterranean Basin and Middle East from direct-sun AERONET observations, Atmos. Chem. Phys., 9, 8265–8282, https://doi.org/10.5194/acp-9-8265-2009, 2009.

Bergstrom, R. W.: Predictions of the spectral absorption and extinction coefficients of an urban air pollution aerosol model, Atmos. Environ., 6, 247–258, https://doi.org/10.1016/0004-6981(72)90083-2, 1972.

Bergstrom, R. W.: Extinction and absorption coefficients of the atmospheric aerosol as a function of particle size, Beiträge zur Physik der Atmosphäre, 46, 223–234, 1973.

Bergstrom, R. W., Russell, P. B., and Hignett, P.: Wavelength dependence of the absorption of black carbon particles: Predictions and results from the TARFOX experiment and implications for the aerosol single scattering albedo, J. Atmos. Sci., 59, 567–577, https://doi.org/10.1175/1520-0469(2002)059<0567:WDOTAO>2.0.CO;2, 2002.

Bergstrom, R. W., Pilewskie, P., Pommier, J., Rabbette, M., Russell, P. B., Schmid, B., Redemann, J., Higurashi, A., Nakajima, T., and Quinn, P. K.: Spectral absorption of solar radiation by aerosols during ACE-Asia, J. Geophys. Res., 109, D19S15, https://doi.org/10.1029/2003JD004467, 2004.

Bergstrom, R. W., Pilewskie, P., Russell, P. B., Redemann, J., Bond, T. C., Quinn, P. K., and Sierau, B.: Spectral absorption properties of atmospheric aerosols, Atmos. Chem. Phys., 7, 5937–5943, https://doi.org/10.5194/acp-7-5937-2007, 2007.

Bergstrom, R. W., Schmidt, K. S., Coddington, O., Pilewskie, P., Guan, H., Livingston, J. M., Redemann, J., and Russell, P. B.: Aerosol spectral absorption in the Mexico City area: results from airborne measurements during MILAGRO/INTEX B, Atmos. Chem. Phys., 10, 6333–6343, https://doi.org/10.5194/acp-10-6333-2010, 2010.

Bohren, C. F. and Huffman, D. R.: Absorption and scattering of light by small particles, John Wiley, Hoboken, N.J., 1983.

Bond, T. C.: Spectral dependence of visible light absorption by carbonaceous particles emitted from coal combustion, Geophys. Res. Lett., 28(21), 4075–4078, https://doi.org/10.1029/2001GL013652, 2001.

Bond, T. C. and Bergstrom, R. W.: Light absorption by carbonaceous particles: An investigative review, Aerosol Sci. Tech., 40, 27–67, https://doi.org/10.1080/02786820500421521, 2006.

Cattrall, C., Carder, K. L., and Gordon, H. R.: Columnar aerosol single-scattering albedo and phase function retrieved from sky radiance over the ocean: Measurements of Saharan dust, J. Geophys. Res., 108, 4287, https://doi.org/10.1029/2002jd002497, 2003.

Chandrasekhar, S.: Radiative trasnfer, New York Publishers, ISBN: 9780486605906, 1960.

Chaudhry, Z., Martins, J. V., Li, Z., Tsay, S. C., Chen, H., Wang, P., Wen, T., Li, C., and Dickerson, R. R.: In situ measurements of aerosol mass concentration and radiative properties in Xianghe, southeast of Beijing, J. Geophys. Res., 112, D23S90, https://doi.org/10.1029/2007JD009055, 2007.

Chyacutelek, P. and Coakley, J. A.: Aerosols and climate, Science, 183, 75–77, https://doi.org/10.1126/science.183.4120.75, 1974.

Clarke, A., McNaughton, C., Kapustin, V., Shinozuka, Y., Howell, S., Dibb, J., Zhou, J., Anderson, B. E., Brekhovskikh, V., Turner, H., and Pinkerton, M.: Biomass burning and pollution aerosol over North America: Organic components and their influence on spectral optical properties and humidification response, J. Geophys. Res., 112, D12S18, https://doi.org/10.1029/2006JD007777, 2007.

Clarke, A. D., Noone, K. J., Heintzenberg, J., Warren, S. G., and Covert, D. S.: Aerosol light absorption measurement techniques: Analysis and intercomparisons, Atmos. Environ., 21, 1455–1465, https://doi.org/10.1016/0004-6981(67)90093-5, 1967.

Colarco, P. R., Gassó, S., Ahn, C., Buchard, V., da Silva, A. M., and Torres, O.: Simulation of the Ozone Monitoring Instrument aerosol index using the NASA Goddard Earth Observing System aerosol reanalysis products, Atmos. Meas. Tech., 10, 4121–4134, https://doi.org/10.5194/amt-10-4121-2017, 2017.

Collaud Coen, M., Weingartner, E., Apituley, A., Ceburnis, D., Fierz-Schmidhauser, R., Flentje, H., Henzing, J. S., Jennings, S. G., Moerman, M., Petzold, A., Schmid, O., and Baltensperger, U.: Minimizing light absorption measurement artifacts of the Aethalometer: evaluation of five correction algorithms, Atmos. Meas. Tech., 3, 457–474, https://doi.org/10.5194/amt-3-457-2010, 2010.

Di Biagio, C., Formenti, P., Balkanski, Y., Caponi, L., Cazaunau, M., Pangui, E., Journet, E., Nowak, S., Andreae, M. O., Kandler, K., Saeed, T., Piketh, S., Seibert, D., Williams, E., and Doussin, J.-F.: Complex refractive indices and single-scattering albedo of global dust aerosols in the shortwave spectrum and relationship to size and iron content, Atmos. Chem. Phys., 19, 15503–15531, https://doi.org/10.5194/acp-19-15503-2019, 2019.

Dubovik, O. and King, M. D.: A flexible inversion algorithm for retrieval of aerosol optical properties from Sun and sky radiance measurements, J. Geophys. Res., 105, 20673–20696, https://doi.org/10.1029/2000JD900282, 2000.

Dubovik, O., Holben, B. N., Kaufman, Y. J., Yamasoe, M., Smimov, A., Tanré, D., and Slutsker, I.: Single-scattering albedo of smoke retrieved from the sky radiance and solar transmittance measured from ground, J. Geophys. Res., 103, 31903–31923, https://doi.org/10.1029/98JD02276, 1998.

Dubovik, O., Smirnov, A., Holben, B. N., King, M. D., Kaufman, Y. J., Eck, T. F., and Slutsker, I.: Accuracy assessments of aerosol optical properties retrieved from Aerosol Robotic Network (AERONET) Sun and sky radiance measurements, J. Geophys. Res., 105, 9791–9806, https://doi.org/10.1029/2000JD900040, 2000.

Dubovik, O., Sinyuk, A., Lapyonok, T., Holben, B. N., Mishchenko, M., Yang, P., Eck, T. F., Volten, H., Muñoz, O., Veihelmann, B., van der Zande, W. J., Leon, J. F., Sorokin, M., and Slutsker, I.: Application of spheroid models to account for aerosol particle nonsphericity in remote sensing of desert dust, J. Geophys. Res., 111, D11208, https://doi.org/10.1029/2005JD006619, 2006.

Eck, T. F., Holben, B. N., Slutsker, I., and Setzer, A.: Measurements of irradiance attenuation and estimation of aerosol single scattering albedo for biomass burning aerosols in Amazonia, J. Geophys. Res., 103, 31865–31878, https://doi.org/10.1029/98JD00399, 1998.

Eck, T. F., Holben, B. N., Reid, J. S., Dubovik, O., Smirnov, A., O'Neill, N. T., Slutsker, I., and Kinne, S.: Wavelength dependence of the optical depth of biomass burning, urban, and desert dust aerosols, J. Geophys. Res., 104, 31333–31349, https://doi.org/10.1029/1999JD900923, 1999.

Eck, T. F., Holben, B. N., Ward, D. E., Dubovik, O., Reid, J. S., Smirnov, A., Mukelabai, M. M., Hsu, N. C., O'Neill, N. T., and Slutsker, I.: Characterization of the optical properties of biomass burning aerosols in Zambia during the 1997 ZIBBEE field campaign, J. Geophys. Res., 106, 3425–3448, https://doi.org/10.1029/2000JD900555, 2001.

Eck, T. F., Holben, B. N., Ward, D. E., Mukelabai, M. M., Dubovik, O., Smirnov, A., Schafer, J. S., Hsu, N. C., Piketh, S. J., Queface, A., Le Roux, J., Swap, R. J., and Slutsker, I.: Variability of biomass burning aerosol optical characteristics in southern Africa during the SAFARI 2000 dry season campaign and a comparison of single scattering albedo estimates from radiometric measurements, J. Geophys. Res., 108, 8477, https://doi.org/10.1029/2002JD002321, 2003.

Eck, T. F., Holben, B. N., Sinyuk, A., Pinker, R. T., Goloub, P., Chen, H., Chatenet, B., Li, Z., Singh, R. P., Tripathi, S. N., Reid, J. S., Giles, D. M., Dubovik, O., O'Neill, N. T., Smirnov, A., Wang, P., and Xia, X.: Climatological aspects of the optical properties of fine/coarse mode aerosol mixtures, J. Geophys. Res., 115, D19205, https://doi.org/10.1029/2010JD014002, 2010.

Eck, T. F., Holben, B. N., Reid, J. S., Mukelabai, M. M., Piketh, S. J., Torres, O., Jethva, H. T., Hyer, E. J., Ward, D. E., Dubovik, O., Sinyuk, A., Schafer, J. S., Giles, D. M., Sorokin, M., Smirnov, A., and Slutsker, I.: A seasonal trend of single scattering albedo in southern African biomass-burning particles: Implications for satellite products and estimates of emissions for the world's largest biomass-burning source, J. Geophys. Res.-Atmos., 118, 6414–6432, https://doi.org/10.1002/jgrd.50500, 2013.

El-Metwally, M., Alfaro, S. C., Abdel Wahab, M., and Chatenet, B.: Aerosol characteristics over urban Cairo: Seasonal variations as retrieved from Sun photometer measurements, J. Geophys. Res., 113, D14219, https://doi.org/10.1029/2008JD009834, 2008.

Fraser, R. S. and Kaufman, Y. J.: The relative importance of aerosol scattering and absorption in remote sensing, IEEE T. Geosci. Remote, GE-23, 625–633, https://doi.org/10.1109/TGRS.1985.289380, 1985.

Giles, D. M., Holben, B. N., Eck, T. F., Sinyuk, A., Smirnov, A., Slutsker, I., Dickerson, R. R., Thompson, A. M., and Schafer, J. S.: An analysis of AERONET aerosol absorption properties and classifications representative of aerosol source regions, J. Geophys. Res., 117, D17203, https://doi.org/10.1029/2012JD018127, 2012.

Giles, D. M., Sinyuk, A., Sorokin, M. G., Schafer, J. S., Smirnov, A., Slutsker, I., Eck, T. F., Holben, B. N., Lewis, J. R., Campbell, J. R., Welton, E. J., Korkin, S. V., and Lyapustin, A. I.: Advancements in the Aerosol Robotic Network (AERONET) Version 3 database – automated near-real-time quality control algorithm with improved cloud screening for Sun photometer aerosol optical depth (AOD) measurements, Atmos. Meas. Tech., 12, 169–209, https://doi.org/10.5194/amt-12-169-2019, 2019.

Guenther, B., Xiong, X., Salomonson, V. V., Barnes, W. L., and Young, J.: On-orbit performance of the earth observing system Moderate Resolution Imaging Spectroradiometer: First year of data, Remote Sens. Environ., 83, 16–30, https://doi.org/10.1016/S0034-4257(02)00097-4, 2002.

Hansen, J., Sato, M., and Ruedy, R.: Radiative forcing and climate response, J. Geophys. Res., 102, 6831–6864, https://doi.org/10.1029/96JD03436, 1997.

Heintzenberg, J., Charlson, R. J., Clarke, A. D., Liousse, C., Ramaswamy, V., Shine, K. P., Wendisch, M., and Helas, G.: Measurements and modelling of aerosol single-scattering albedo: Progress, problems and prospects, Contributions to Atmospheric Physics, 70, 249–263, 1997.

Herman, B. M. and Browning, S. R.: A numerical solution to the equation of radiative transfer, J. Atmos. Sci., 22, 559–566, https://doi.org/10.1175/1520-0469(1965)022<0559:ANSTTE>2.0.CO;2, 1965.

Holben, B. N., Eck, T. F., Slutsker, I., Tanré, D., Buis, J. P., Setzer, A., Vermote, E., Reagan, J. A., Kaufman, Y. J., Nakajima, T., Lavenu, F., Jankowiak, I., and Smirnov, A.: AERONET – A federated instrument network and data archive for aerosol characterization, Remote Sens. Environ., 66, 1–16, https://doi.org/10.1016/S0034-4257(98)00031-5, 1998.

Hsu, N. C., Jeong, M. J., Bettenhausen, C., Sayer, A. M., Hansell, R., Seftor, C. S., Huang, J., and Tsay, S. C.: Enhanced Deep Blue aerosol retrieval algorithm: The second generation, J. Geophys. Res.-Atmos., 118, 9296–9315, https://doi.org/10.1002/jgrd.50712, 2013.

IPCC: Intergovernmental Panel on Climate Change: The physical science basis: contribution of working group I to the fifth assessment report of the Intergovernmental Panel on Climate Change, in: Climate Change, edited by: Stocker, T. F., Qin, D., Plattner, G. K., Tignor, M., Allen, S. K., Boschung, J., Nauels, A., Xia, Y., Bex, V., and Midgley, P. M., Cambridge University Press, p. 1535, ISBN: 9781107661820, 2013.

Jethva, H. and Torres, O.: Satellite-based evidence of wavelength-dependent aerosol absorption in biomass burning smoke inferred from Ozone Monitoring Instrument, Atmos. Chem. Phys., 11, 10541–10551, https://doi.org/10.5194/acp-11-10541-2011, 2011.

Jethva, H. and Torres, O.: A comparative evaluation of Aura-OMI and SKYNET near-UV single-scattering albedo products, Atmos. Meas. Tech., 12, 6489–6503, https://doi.org/10.5194/amt-12-6489-2019, 2019.

Jethva, H., Torres, O., and Ahn, C.: Global assessment of OMI aerosol single-scattering albedo using ground-based AERONET inversion, J. Geophys. Res.-Atmos., 119, 9020–9040, https://doi.org/10.1002/2014JD021672, 2014.

Kaufman, Y. J.: Satellite sensing of aerosol absorption, J. Geophys. Res., 92, 4307–4317, https://doi.org/10.1029/JD092iD04p04307, 1987.

Kaufman, Y. J., Martins, J. V., Remer, L. A., Schoeberl, M. R., and Yamasoe, M. A.: Satellite retrieval of aerosol absorption over the oceans using sunglint, Geophys. Res. Lett., 29, 1928, https://doi.org/10.1029/2002gl015403, 2002.

King, M. D., Kaufman, Y. J., Menzel, W. P., and Tanré, D.: Remote sensing of cloud, aerosol, and water vapor properties from

the Moderate Resolution Imaging Spectrometer (MODIS), IEEE T. Geosci. Remote, 30, 2–27, https://doi.org/10.1109/36.124212, 1992.

Kirchstetter, T. W., Novakov, T., and Hobbs, P. V.: Evidence that the spectral dependence of light absorption by aerosols is affected by organic carbon, J. Geophys. Res., 109, D21208, https://doi.org/10.1029/2004JD004999, 2004.

Krotkov, N. A., Herman, J. R., Cede, A., and Labow, G.: Partitioning between aerosol and NO_2 absorption in the UV spectral region, in: Ultraviolet Ground- and Space-based Measurements, Models, and Effects V, edited by: Bernhard, G., Slusser, J. R., Herman, J. R., and Gao, W., p. 588601, https://doi.org/10.1117/12.615285, 2005.

Lee, K. H., Li, Z., Wong, M. S., Xin, J., Wang, Y., Hao, W. M., and Zhao, F.: Aerosol single scattering albedo estimated across China from a combination of ground and satellite measurements, J. Geophys. Res., 112, D22S15, https://doi.org/10.1029/2007JD009077, 2007.

Levelt, P. F., van den Oord, G. H. J., Dobber, M. R., Mälkki, A., Visser, H., de Vries, J., Stammes, P., Lundell, J. O. V., and Saari, H.: The Ozone Monitoring Instrument, IEEE T. Geosci. Remote, 44, 1093–1101, https://doi.org/10.1109/TGRS.2006.872333, 2006.

Levy, R. C., Remer, L. A., Mattoo, S., Vermote, E. F., and Kaufman, Y. J.: Second-generation operational algorithm: Retrieval of aerosol properties over land from inversion of Moderate Resolution Imaging Spectroradiometer spectral reflectance, J. Geophys. Res., 112, D13211, https://doi.org/10.1029/2006JD007811, 2007.

Li, C., Marufu, L. T., Dickerson, R. R., Li, Z., Wen, T., Wang, Y., Wang, P., Chen, H., and Stehr, J. W.: In situ measurements of trace gases and aerosol optical properties at a rural site in northern China during East Asian Study of Tropospheric Aerosols: An International Regional Experiment 2005, J. Geophys. Res., 112, D22S04, https://doi.org/10.1029/2006JD007592, 2007.

Li, X., Christopher, S. A., Zhang, J., Chou, J., and Welch, R. M.: Aerosol single-scattering albedo estimated from NOAA-14 AVHRR measurements: case studies over Brazil, in Proc. SPIE 3756, Optical Spectroscopic Techniques and Instrumentation for Atmospheric and Space Research III, Denver, CO, USA, 20 October 1999, https://doi.org/10.1117/12.366393, 1999.

Li, Z., Zhao, X., Kahn, R., Mishchenko, M., Remer, L., Lee, K.-H., Wang, M., Laszlo, I., Nakajima, T., and Maring, H.: Uncertainties in satellite remote sensing of aerosols and impact on monitoring its long-term trend: a review and perspective, Ann. Geophys., 27, 2755–2770, https://doi.org/10.5194/angeo-27-2755-2009, 2009.

Lyapustin, A. and Wang, Y.: MCD19A1 MODIS/Terra+Aqua Land Surface BRF Daily L2G Global 500m and 1km SIN Grid V006, NASA EOSDIS Land Processes DAAC, [data set], https://doi.org/10.5067/MODIS/MCD19A1.006, 2018.

Lyapustin, A., Smirnov, A., Holben, B., Chin, M., Streets, D. G., Lu, Z., Kahn, R., Slutsker, I., Laszlo, I., Kondragunta, S., Tanré, D., Dubovik, O., Goloub, P., Chen, H.-B., Sinyuk, A., Wang, Y., and Korkin, S.: Reduction of aerosol absorption in Beijing since 2007 from MODIS and AERONET, Geophys. Res. Lett., 38, L10803, https://doi.org/10.1029/2011gl047306, 2011.

Lyapustin, A., Wang, Y., Korkin, S., and Huang, D.: MODIS Collection 6 MAIAC algorithm, Atmos. Meas. Tech., 11, 5741–5765, https://doi.org/10.5194/amt-11-5741-2018, 2018.

Mallet, M., Dubovik, O., Nabat, P., Dulac, F., Kahn, R., Sciare, J., Paronis, D., and Léon, J. F.: Absorption properties of Mediterranean aerosols obtained from multi-year ground-based remote sensing observations, Atmos. Chem. Phys., 13, 9195–9210, https://doi.org/10.5194/acp-13-9195-2013, 2013.

Martins, J. V., Artaxo, P., Kaufman, Y. J., Castanho, A. D., and Remer, L. A.: Spectral absorption properties of aerosol particles from 350–2500 nm, Geophys. Res. Lett., 36, L13810, https://doi.org/10.1029/2009GL037435, 2009.

Mitchell, R. M., Forgan, B. W., Campbell, S. K., and Qin, Y.: The climatology of Australian tropical aerosol: Evidence for regional correlation, Geophys. Res. Lett., 40, 2384–2389, https://doi.org/10.1002/grl.50403, 2013.

Moosmüller, H., Chakrabarty, R. K., and Arnott, W. P.: Aerosol light absorption and its measurement: A review, J. Quant. Spectrosc. Ra., 110, 844–878, https://doi.org/10.1016/j.jqsrt.2009.02.035, 2009.

Müller, T., Schladitz, A., Massling, A., Kaaden, N., Kandler, K., and Wiedensohler, A.: Spectral absorption coefficients and imaginary parts of refractive indices of Saharan dust during SAMUM-1, Tellus B, 61, 79–95, https://doi.org/10.1111/j.1600-0889.2008.00399.x, 2009.

Nakajima, T., Tonna, G., Rao, R., Boi, P., Kaufman, Y., and Holben, B.: Use of sky brightness measurements from ground for remote sensing of particulate polydispersions, Appl. Optics, 35, 2672–2686, https://doi.org/10.1364/ao.35.002672, 1996.

Nakajima, T., Yoon, S., Ramanathan, V., Shi, G. Y., Takemura, T., Higurashi, A., Takamura, T., Aoki, K., Sohn, B. J., Kim, S. W., Tsuruta, H., Sugimoto, N., Shimizu, A., Tanimoto, H., Sawa, Y., Lin, N. H., Lee, C. T., Goto, D., and Schutgens, N.: Overview of the Atmospheric Brown Cloud East Asian Regional Experiment 2005 and a study of the aerosol direct radiative forcing in east Asia, J. Geophys. Res., 112, D24S91, https://doi.org/10.1029/2007JD009009, 2007.

Petzold, A., Rasp, K., Weinzierl, B., Esselborn, M., Hamburger, T., Dörnbrack, A., Kandler, K., Schütz, L., Knippertz, P., Fiebig, M., and Virkkula, A.: Saharan dust absorption and refractive index from aircraft-based observations during SAMUM 2006, Tellus B, 61, 118–130, https://doi.org/10.1111/j.1600-0889.2008.00383.x, 2009.

Putaud, J. P., Cavalli, F., Martins dos Santos, S., and Dell'Acqua, A.: Long-term trends in aerosol optical characteristics in the Po Valley, Italy, Atmos. Chem. Phys., 14, 9129–9136, https://doi.org/10.5194/acp-14-9129-2014, 2014.

Reid, J. S. and Hobbs, P. V.: Physical and optical properties of young smoke from individual biomass fires in Brazil, J. Geophys. Res., 103, 32013–32030, https://doi.org/10.1029/98JD00159, 1998.

Reid, J. S., Hobbs, P. V., Ferek, R. J., Blake, D. R., Martins, J. V., Dunlap, M. R., and Lioussse, C.: Physical, chemical, and optical properties of regional hazes dominated by smoke in Brazil, J. Geophys. Res., 103, 32059–32080, https://doi.org/10.1029/98JD00458, 1998.

Remer, L. A., Kaufman, Y. J., Tanré, D., Mattoo, S., Chu, D. A., Martins, J. V., Li, R. R., Ichoku, C., Levy, R. C., Kleidman, R. G., Eck, T. F., Vermote, E., and Holben, B. N.: The MODIS aerosol

algorithm, products, and validation, J. Atmos. Sci., 62, 947–973, https://doi.org/10.1175/JAS3385.1, 2005.

Satheesh, S. K. and Srinivasan, J.: A method to infer shortwave absorption due to aerosols using satellite remote sensing, Geophys. Res. Lett., 32, L13814, https://doi.org/10.1029/2005GL023064, 2005.

Schafer, J. S., Eck, T. F., Holben, B. N., Artaxo, P., and Duarte, A. F.: Characterization of the optical properties of atmospheric aerosols in Amazônia from long-term AERONET monitoring (1993–1995 and 1999–2006), J. Geophys. Res., 113, D04204, https://doi.org/10.1029/2007JD009319, 2008.

Schenkeveld, V. M. E., Jaross, G., Marchenko, S., Haffner, D., Kleipool, Q. L., Rozemeijer, N. C., Veefkind, J. P., and Levelt, P. F.: In-flight performance of the Ozone Monitoring Instrument, Atmos. Meas. Tech., 10, 1957–1986, https://doi.org/10.5194/amt-10-1957-2017, 2017.

Schnaiter, M., Schmid, O., Petzold, A., Fritzsche, L., Klein, K. F., Andreae, M. O., Helas, G., Thielmann, A., Gimmler, M., Möhler, O., Linke, C., and Schurath, U.: Measurement of wavelength-resolved light absorption by aerosols utilizing a UV-VIS extinction cell, Aerosol Sci. Tech., 39, 249–260, https://doi.org/10.1080/027868290925958, 2005.

Scott, W. D., Forgan, B. W., and Prospero, J. M.: Atmospheric turbidity measurements at Broome in Western Australia 1979–1984, Journal of the Royal Society of Western Australia, 75, 111–118, 1992.

Selimovic, V., Yokelson, R. J., McMeeking, G. R., and Coefield, S.: Aerosol mass and optical properties, smoke influence on O_3, and high NO_3 production rates in a Western U.S. City impacted by wildfires, J. Geophys. Res.-Atmos., 125, e2020JD032791, https://doi.org/10.1029/2020JD032791, 2020.

Sinyuk, A., Torres, O., and Dubovik, O.: Combined use of satellite and surface observations to infer the imaginary part of refractive index of Saharan dust, Geophys. Res. Lett., 30, 1081, https://doi.org/10.1029/2002GL016189, 2003.

Sinyuk, A., Holben, B. N., Eck, T. F., Giles, D. M., Slutsker, I., Korkin, S., Schafer, J. S., Smirnov, A., Sorokin, M., and Lyapustin, A.: The AERONET Version 3 aerosol retrieval algorithm, associated uncertainties and comparisons to Version 2, Atmos. Meas. Tech., 13, 3375–3411, https://doi.org/10.5194/amt-13-3375-2020, 2020.

Sokolik, I. N. and Toon, O. B.: Direct radiative forcing by anthropogenic airborne mineral aerosols, Nature, 381, 681–683, https://doi.org/10.1038/381681a0, 1996.

Sokolik, I. N. and Toon, O. B.: Incorporation of mineralogical composition into models of the radiative properties of mineral aerosol from UV to IR wavelengths, J. Geophys. Res., 104, 9423–9444, https://doi.org/10.1029/1998JD200048, 1999.

Torres, O., Bhartia, P. K., Herman, J. R., Ahmad, Z., and Gleason, J.: Derivation of aerosol properties from satellite measurements of backscattered ultraviolet radiation: Theoretical basis, J. Geophys. Res., 103, 17099–17110, https://doi.org/10.1029/98JD00900, 1998.

Torres, O., Tanskanen, A., Veihelmann, B., Ahn, C., Braak, R., Bhartia, P. K., Veefkind, P., and Levelt, P.: Aerosols and surface UV products form Ozone Monitoring Instrument observations: An overview, J. Geophys. Res., 112, D24S47, https://doi.org/10.1029/2007JD008809, 2007.

Torres, O., Ahn, C., and Chen, Z.: Improvements to the OMI near-UV aerosol algorithm using A-train CALIOP and AIRS observations, Atmos. Meas. Tech., 6, 3257–3270, https://doi.org/10.5194/amt-6-3257-2013, 2013.

Torres, O., Bhartia, P. K., Jethva, H., and Ahn, C.: Impact of the ozone monitoring instrument row anomaly on the long-term record of aerosol products, Atmos. Meas. Tech., 11, 2701–2715, https://doi.org/10.5194/amt-11-2701-2018, 2018.

Vandaele, A. C., Hermans, C., Simon, P. C., Carleer, M., Colin, R., Fally, S., Mérienne, M. F., Jenouvrier, A., and Coquart, B.: Measurements of the NO_2 absorption cross-section from $42\,000\,cm^{-1}$ to $10\,000\,cm^{-1}$ (238–1000 nm) at 220 K and 294 K, J. Quant. Spectrosc. Ra., 59, 171–184, https://doi.org/10.1016/S0022-4073(97)00168-4, 1998.

van de Hulst, H. C.: Light scattering by small particles, John Wiley and Sons, New York, ISBN: 0486642283, 1957.

Virkkula, A., Ahlquist, N. C., Covert, D. S., Arnott, W. P., Sheridan, P. J., Quinn, P. K., and Coffman, D. J.: Modification, calibration and a field test of an instrument for measuring light absorption by particles, Aerosol Sci. Tech., 39, 68–83, https://doi.org/10.1080/027868290901963, 2005.

Ward, D. E.: Smoke and fire characteristics for cerrado and deforestation burns in Brazil: BASE-B experiment, J. Geophys. Res., 97, 14601–14619, https://doi.org/10.1029/92jd01218, 1992.

Weingartner, E., Saathoff, H., Schnaiter, M., Streit, N., Bitnar, B., and Baltensperger, U.: Absorption of light by soot particles: Determination of the absorption coefficient by means of aethalometers, J. Aerosol Sci., 34, 1445–1463, https://doi.org/10.1016/S0021-8502(03)00359-8, 2003.

Xiong, X., Angal, A., Barnes, W. L., Chen, H., Chiang, V., Geng, X., Li, Y., Twedt, K., Wang, Z., Wilson, T., and Wu, A.: Updates of Moderate Resolution Imaging Spectroradiometer on-orbit calibration uncertainty assessments, J. Appl. Remote Sens., 12, 034001, https://doi.org/10.1117/1.jrs.12.034001, 2018.

Zhu, L., Martins, J. V., and Remer, L. A.: Biomass burning aerosol absorption measurements with MODIS using the critical reflectance method, J. Geophys. Res., 116, D07202, https://doi.org/10.1029/2010JD015187, 2011.